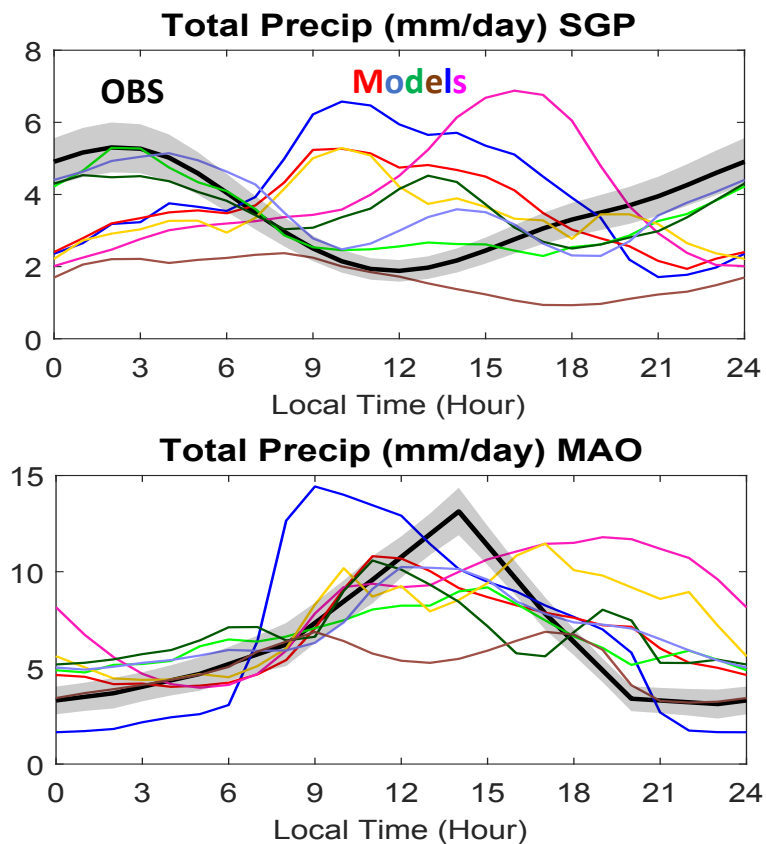


## Long-Term Single-Column Model Intercomparison on the Diurnal Cycle of Precipitation Over Midlatitude and Tropical Land

Shuaiqi Tang, Shaocheng Xie\*, Zhun Guo, Song-You Hong, Boualem Khouider, Daniel Klocke, Martin Köhler, Myung-Seo Koo, Phani Murali Krishna, Vincent E. Larson, Sungsu Park, Paul A. Vaillancourt, Yi-Chi Wang, Jing Yang, Chimene Laure Daleu, Cameron R. Homeyer, Todd R. Jones, Neelam Malap, Roel Neggers, Thara Prabhakaran, Enver Ramirez, Courtney Schumacher, Cheng Tao, Peter Bechtold, Hsi-Yen Ma, J. David Neelin, and Xubin Zeng

Eleven single-column models are used to study the diurnal cycle of precipitation and related physical processes over two continental sites SGP and MAO. Most models produce afternoon precipitation too early, likely due to the missing transition of shallow-to-deep convection in the models. Many models cannot produce convection occurring at nighttime. Unified treatment of shallow and deep convection and the capability to capture mid-level convection are important for models to capture diurnal cycle of precipitation.



# 1 Long-Term Single-Column Model Intercomparison on the Diurnal 2 Cycle of Precipitation Over Midlatitude and Tropical Land

3  
4  
5  
6  
7  
8  
9  
10 Shuaiqi Tang<sup>1</sup>, Shaocheng Xie<sup>2\*</sup>, Zhun Guo<sup>3</sup>, Song-You Hong<sup>4</sup>, Boualem Khouider<sup>5</sup>, Daniel  
11 Klocke<sup>6#</sup>, Martin Köhler<sup>7</sup>, Myung-Seo Koo<sup>8</sup>, Phani Murali Krishna<sup>9</sup>, Vincent E. Larson<sup>10,1</sup>,  
12 Sungsu Park<sup>11</sup>, Paul A. Vaillancourt<sup>12</sup>, Yi-Chi Wang<sup>13</sup>, Jing Yang<sup>12</sup>, Chimene Laure Daleu<sup>14</sup>,  
13 Cameron R. Homeyer<sup>15</sup>, Todd R. Jones<sup>14</sup>, Neelam Malap<sup>9</sup>, Roel Neggers<sup>16</sup>, Thara Prabhakaran<sup>9</sup>,  
14 Enver Ramirez<sup>17</sup>, Courtney Schumacher<sup>18</sup>, Cheng Tao<sup>2</sup>, Peter Bechtold<sup>19</sup>, Hsi-Yen Ma<sup>2</sup>, J. David  
15 Neelin<sup>20</sup>, and Xubin Zeng<sup>21</sup>

- 16 10
- 17 11
- 18 12
- 19 13
- 20 13 1. Pacific Northwest National Laboratory, Richland, WA, USA
- 21 14 2. Lawrence Livermore National Laboratory, Livermore, CA, USA
- 22 15
- 23 15 3. Climate Change Research Center, Institute of Atmospheric Physics, Chinese Academy of  
24 16 Sciences, Beijing, China.
- 25 16
- 26 17 4. NOAA/Earth System Research Laboratory and CIRES/University of Colorado, Boulder,  
27 18 CO, USA
- 28 18
- 29 19 5. Department of Mathematics and Statistics, University of Victoria, Victoria, BC, Canada
- 30 20 6. Hans Ertel Centre for Weather Research, Deutscher Wetterdienst, Offenbach, Germany
- 31 20
- 32 21 7. Deutscher Wetterdienst, Offenbach, Germany
- 33 21
- 34 22 8. Korea Institute of Atmospheric Prediction Systems, Seoul, South Korea
- 35 23 9. Indian Institute of Tropical Meteorology, Pune, India
- 36 23
- 37 24 10. Department of Mathematical Sciences, University of Wisconsin-Milwaukee, Milwaukee,  
38 25 WI, USA
- 39 25
- 40 26 11. School of Earth and Environmental Sciences, Seoul National University, Seoul, South  
41 27 Korea
- 42 27
- 43 28 12. Meteorology Research Division, Environment and Climate Change Canada, Dorval,  
44 29 Québec, Canada
- 45 29
- 46 30 13. Research Center for Environmental Changes, Academia Sinica, Taipei, Taiwan
- 47 31 14. Department of Meteorology, University of Reading, Reading, UK.
- 48 31
- 49 32 15. School of Meteorology, University of Oklahoma, Norman, OK, USA
- 50 32
- 51 33 16. Institute of Geophysics and Meteorology, University of Cologne, Cologne, Germany
- 52 33
- 53 34 17. Numerical Modeling and Development Division, Center for Weather Forecasting and  
54 35 Climate Studies, National Institute for Space Research, São Paulo, Brazil
- 55 36 18. Department of Atmospheric Sciences, Texas A&M University, College Station, TX, USA
- 56 36
- 57
- 58
- 59
- 60

- 1  
2  
3 37 19. European Centre for Medium-Range Weather Forecasts, Reading, UK  
4  
5 38 20. Dept. of Atmospheric and Oceanic Sciences, University of California in Los Angeles,  
6 39 Los Angeles, CA, USA  
7  
8 40 21. Department of Hydrology and Atmospheric Sciences, University of Arizona, Tucson,  
9 41 AZ, USA

10 42

11  
12 43 # now at Max-Planck-Institut für Meteorologie, Hamburg, Germany  
13

14 44

15  
16 45

17  
18 46

19  
20 47

21  
22 48

23  
24 49

25  
26 50

27  
28 51

29  
30 52

31  
32 53

33  
34 54

35  
36 55

37  
38  
39  
40 56 Contact: Shaocheng Xie ([xie2@llnl.gov](mailto:xie2@llnl.gov))  
41

42 57  
43  
44  
45  
46  
47  
48  
49  
50  
51  
52  
53  
54  
55  
56  
57  
58  
59  
60

58

## Abstract

59 General Circulation Models (GCMs) have for decades exhibited difficulties in modeling the  
60 diurnal cycle of precipitation (DCP). This issue can be related to inappropriate representation of  
61 the processes controlling sub-diurnal phenomena like convection. In this study, eleven single-  
62 column versions of GCMs are used to investigate the interactions between convection and  
63 environmental conditions, processes that control nocturnal convections, and the transition from  
64 shallow to deep convection on diurnal time scale. Long-term simulations are performed over two  
65 continental land sites: the Southern Great Plains (SGP) in the U.S. for twelve summer months  
66 from 2004 to 2015 and the Manacapuru site at the central Amazon (MAO) in Brazil for two full  
67 years from 2014 to 2015. The analysis is done on two regimes: afternoon convective regime and  
68 nocturnal precipitation regime. Most models produce afternoon precipitation too early, likely due  
69 to the missing transition of shallow-to-deep convection in these models. At SGP, the unified  
70 convection schemes better simulate the onset time of precipitation. At MAO, models produce  
71 heating peak in a much lower level comparing with observation, indicating too shallow  
72 convection in the models. For nocturnal precipitation, models that produce most of nocturnal  
73 precipitation all allow convection to be triggered above the boundary layer. This indicates the  
74 importance of model capability to detect elevated convection for simulating nocturnal  
75 precipitation. Sensitivity studies indicate that (1) nudging environmental variables towards  
76 observations has a minor impact on the diurnal cycle of precipitation; (2) unified treatment of  
77 shallow and deep convection and the capability to capture mid-level convection are important for  
78 models to capture DCP; and (3) the interactions of the atmosphere with other components in the  
79 climate system (e.g., land) are also important for DCP simulations in coupled models. These  
80 results provide long-term statistical insights on which physical processes are essential in climate  
81 models to simulate DCP.

82

## 1. Introduction

The diurnal cycle of precipitation (DCP) is one of the most important signals affecting climate variability and weather forecasting. Although it is dominated by diurnal variation of solar insolation that greatly affects the surface energy budget and regulates surface temperature (Dai et al. 1999), mesoscale propagating systems and large scale envelopes are also responsible to regulate the DCP (e.g., Rutledge and Hobbs 1984; Wei et al. 2020). As a benchmark for evaluating climate models (Covey et al. 2016), DCP provides an excellent measure of how well climate models simulate not only the total amount of precipitation but also its frequency, intensity, timing and duration (Trenberth et al. 2003).

General Circulation Models (GCMs) have for decades exhibited difficulties in modeling the diurnal precipitation. Dai (2006) examined 18 GCMs and found that many models showed peak precipitation around noontime over land and around 02 local standard time (LST) over ocean, both a few hours earlier than observations. Covey et al. (2016) examined 24 models from phase 5 of the Coupled Model Intercomparison Project (CMIP5, Taylor et al. 2012), and found similar biases; i.e. GCMs produce warm season rainfall too early in the day. Recently, Fiedler et al. (2020) and Tang et al. (2021) examined the latest GCMs from CMIP6 (Eyring et al. 2016) compared with earlier CMIP versions. They found that although CMIP6 models have made improvements on DCP, they still suffer from the same problems: producing rainfall too early in the day over land and missing nocturnal rainfall peak associated with elevated convection and propagating mesoscale convective systems (MCSs).

These issues in simulating DCP in climate models can be related to inappropriate representation of the processes that control sub-diurnal phenomena like convection, and phenomena with timescales of several hours, like MCSs. Many studies attribute the model biases on DCP to the deficiencies in convective parameterizations (e.g., Koo and Hong 2010). Great efforts have been made to improve DCP in GCMs by improving the convective trigger (e.g., Xie and Zhang 2000; Bechtold et al. 2004; Rio et al. 2009; Wang and Hsu 2019; Xie et al. 2019), closure (e.g., Zhang 2003; Rio et al. 2009; Bechtold et al. 2014), entrainment and detrainment rates (e.g., Wang et al. 2007; Bechtold et al. 2008; Stratton and Stirling 2012), or the detection of mid-level convection that is related to the nocturnal precipitation peak over regions such as the central U.S. (e.g., Lee et al. 2008; Wang et al. 2015; Xie et al. 2019; McTaggart-Cowan et al. 2020). Other parameterizations (e.g., Park 2014a, 2014b; Neggers 2015a; Guo et al. 2021) that unify the deep convective scheme with other parameterizations also provide a path toward improving DCP simulation. The effort of unifying the representation of subgrid-scale convection in GCMs has a long history. One of the serious challenges is that our knowledge of convective physics and dynamics, in particular the limits of applicability of parametric relations that capture observed behavior, is still very limited. This lack of insight is driving intense research into convective transitions, including various recent meteorological field campaigns dedicated to this problem (e.g., CACTI, Varble et al. 2021).

1  
2  
3 121 A single-column model (SCM) is a useful tool to test physical processes within a column of a  
4 122 GCM (Randall et al. 1996; Zhang et al. 2016; Lin and Xie 2021). In the past twenty years,  
5 123 several SCM intercomparison studies have been organized, focusing on summertime continental  
6 124 convection (Ghan et al. 2000; Xie et al. 2002; Guichard et al. 2004), springtime midlatitude  
7 125 frontal clouds (Xie et al. 2005; Xu et al. 2005), shallow-cumulus clouds over mid-latitude land  
8 126 (Lenderink et al. 2004), marine stratocumulus-topped boundary layers (Bretherton et al. 1999;  
9 127 Zhu et al. 2005; Wyant et al. 2007; Neggers et al. 2017), mixed-phase clouds in the polar region  
10 128 (Klein et al. 2009; Morrison et al. 2009; Pithan et al. 2016) and deep convection over the tropical  
11 129 ocean (Bechtold et al. 2000; Davies et al. 2013; Petch et al. 2014). These intercomparison studies  
12 130 serve as testbeds for developing new parameterizations. For DCP, SCMs produce a similar  
13 131 diurnal structure of precipitation as the full 3-D GCM and are thus suitable to be used as a  
14 132 simplified model of GCMs to explore the physical processes related to DCP (Betts and Jakob  
15 133 2002).

16  
17  
18  
19  
20  
21 134 The above-mentioned SCM intercomparison studies mainly focused on case studies. In recent  
22 135 years efforts have been made to pursue longer-term SCM simulations at permanent  
23 136 meteorological sites (Neggers et al. 2012). In certain conditions this allows direct attribution of  
24 137 persistent biases in GCMs to parameterized subgrid-scale processes (Neggers and Siebesma  
25 138 2013; Neggers 2015b). In the recent Global Atmospheric System Studies (GASS) Diurnal Cycle  
26 139 of Precipitation intercomparison project (<https://portal.nersc.gov/project/capt/diurnal/>), we are  
27 140 attempting to build robust statistics of the diurnal cycle of precipitation using long-term  
28 141 simulations from various weather and climate models. Two research sites from the Atmospheric  
29 142 Radiation Measurement (ARM) program, Southern Great Plains (SGP) site in the central U.S.  
30 143 and the Manacapuru (MAO) site for the Green Ocean (GoAmazon2014/5, Martin et al. 2016)  
31 144 experiment in Brazil, are chosen to build the long-term statistics of SCM performance. In  
32 145 addition, a few 1-day cases are selected to use both SCMs and cloud-resolving models (CRMs)  
33 146 for detailed process understanding of model errors in DCP. The goal of this study is to document  
34 147 common model behaviors in simulating the diurnal cycle of precipitation in current weather and  
35 148 climate models by constraining the large-scale conditions in the SCM framework and to provide  
36 149 a benchmark for more in-depth follow-up studies. In particular, this paper will focus on the long-  
37 150 term statistics of the SCM simulations on DCP. More results on SCMs and CRMs for selected  
38 151 cases will be analyzed in a separate paper.

39  
40  
41  
42  
43  
44  
45  
46 152

## 47 48 153 **2. Experimental Design and Participating Models**

49 154

### 50 51 155 2.1 Experimental Design

52  
53 156 Two sets of SCM experiments are designed to build up statistics and connection to climate errors  
54 157 at two continental land locations using a series of short-range 5-day hindcast simulations. The  
55 158 first experiment spans twelve warm seasons (May – August) between 2004 to 2015 at the ARM

1  
2  
3 159 SGP site. The second experiment is two full years from 2014 to 2015 at the ARM MAO site. The  
4 160 default protocol for the SCM simulations is a 5-day non-nudging hindcast, i.e., each SCM is  
5 161 initiated at 00Z every day and runs freely for 5 days without constraining temperature and  
6 162 moisture fields. Compared to typical SCM experiment protocols such as free run (e.g., Ghan et  
7 163 al. 2000) or nudging run, in the hindcast run the large-scale condition will not drift too far away,  
8 164 and the SCM is expected to replicate similar model biases as in GCM (Bogenschutz et al. 2020),  
9 165 so that modelers can identify problems related to parameterizations using SCM hindcast run. In  
10 166 this study, the 24 – 48 hr simulations (day-2 hindcast) are used for analysis. In total there are 123  
11 167 days (1 May to 31 August) per warm season at SGP and 361 days (2 January to 28 December  
12 168 since the 5-day simulations do not cross two years) per year at MAO to build the statistics.

13  
14  
15  
16  
17 169 SCMs are driven with the large-scale forcing derived from the constrained variational analysis  
18 170 (Zhang and Lin 1997; Zhang et al. 2001), which has been widely used in earlier GASS SCM  
19 171 intercomparison studies. The large-scale forcing data at SGP are from the ARM continuous  
20 172 forcing datasets at SGP (Xie et al. 2004; Tang et al. 2019), while the large-scale forcing at MAO  
21 173 are described in Tang et al. (2016). The initial conditions, surface latent and sensible heat fluxes,  
22 174 horizontal winds and the large-scale horizontal and vertical advectons are all prescribed from  
23 175 the large-scale forcing data. Precipitation in the large-scale forcing data, which are from radar  
24 176 measurements averaged within a domain of ~300km in diameter at SGP and ~220km in diameter  
25 177 at MAO, is also used to evaluate model performance.

## 29 30 178 2.2 Participating Models

31  
32 179 Participants in this intercomparison project submitted results from 11 SCMs with all required  
33 180 simulations at SGP and MAO. The basic information of these models is listed in Table 1, and  
34 181 more information about their deep convective parameterizations is listed in Table 2. Note that  
35 182 some of these models have an inheritance relationship with differences in model versions or  
36 183 physical parameterizations. For example, EAMv1 has two other versions: EAMv1.trigger and  
37 184 EAMv1.SILHS, with different deep convective schemes. EAMv1.trigger applies a modified  
38 185 convective trigger that was shown to significantly improve DCP (Xie et al. 2019);  
39 186 EAMv1.SILHS shuts off EAMv1's native deep convective scheme and lets the Cloud Layers  
40 187 Unified By Binormals scheme (CLUBB) treat both shallow and deep convection (Thayer-Calder  
41 188 et al. 2015; Guo et al. 2021), with a Subgrid Importance Latin Hypercube Sampler (SILHS,  
42 189 Larson and Schanen 2013) to interface clouds with microphysics on the subgrid scale. Moreover,  
43 190 SCAM5 is the earlier version of SCAM6, and SAM0-UNICON is developed based on SCAM5  
44 191 with a unified convection scheme (UNICON, Park 2014a, 2014b) for shallow and deep  
45 192 convection. Some models also perform simulations with different model setups or configurations  
46 193 for sensitivity studies. For example, SCAM6 and SKIM perform simulations with an interactive  
47 194 land model; SKIM submitted simulations with atmospheric states nudging to the observations.  
48 195 The variety of simulations allows us to test model sensitivity to parameterizations and model  
49 196 setup. Although models have different vertical and temporal resolution, they are all interpolated

1  
2  
3 197 (or averaged) into 40 vertical levels and 1-hour resolution. The model data are archived and  
4 198 publicly available at <https://portal.neresc.gov/project/mp193/GASS/SCM/data/>.

5  
6  
7 199

### 8 200 **3. Model Performances on the Mean Diurnal Cycle of Precipitation**

9 201

#### 10 202 3.1 General features

11  
12  
13 203 The two ARM sites are located in two distinct but representative environmental conditions: SGP  
14 204 represents typical mid-latitude land condition with upper-level westerlies and dry free  
15 205 troposphere; MAO represents typical tropical rain-forest conditions with warm, moist air in the  
16 206 lower and middle troposphere. A set of diagnostic plots of the meteorological and process-level  
17 207 variables are made available at the GASS-DCP quick-plot webpage  
18 208 ([https://portal.neresc.gov/project/mp193/GASS/SCM/quick\\_plots/](https://portal.neresc.gov/project/mp193/GASS/SCM/quick_plots/)). Due to the length limit, this  
19 209 paper only shows some of them that are closely related to DCP.

20  
21  
22  
23 210 The mean DCP and the harmonic dial plots for the twelve summer seasons at SGP and the two  
24 211 years at MAO are shown in Figure 1. “Harmonic dial plot” (Covey et al. 2016) is a two-  
25 212 dimensional vector diagram in which the radius and angle represent the amplitude and phase,  
26 213 respectively, of the first component of Fourier analysis on the diurnal timeseries (sinusoidal  
27 214 function with period of 24 hours). The observed precipitation at SGP shows a nocturnal  
28 215 precipitation peak after midnight and a daytime minimum at around noon. The diurnal harmonic  
29 216 peak is at around 01 LST. Many models, such as EAMv1, SCAM6, SAM0-UNICON and  
30 217 SMCPCP, produce a precipitation peak during daytime, with harmonic phases between ~11 and  
31 218 15 LST and amplitudes between 1 and 2 mm/day. The failure to produce a nocturnal  
32 219 precipitation peak at SGP is consistent with previous global model studies (e.g., Tang et al.  
33 220 2021). ICON produces early-morning precipitation peak but its magnitude and diurnal amplitude  
34 221 are much lower than the observations. A few models produce a nocturnal precipitation peak,  
35 222 such as SKIM, CMC and TaiESM1. The mechanisms that help these models capturing nocturnal  
36 223 precipitation will be discussed later in Section 3.3.

37  
38  
39  
40  
41  
42  
43 224 The observed precipitation at MAO shows an early afternoon peak with the diurnal harmonic  
44 225 peak just after noon. The precipitation peak is stronger and smoother in the wet season, while it  
45 226 is weaker and sharper in the dry season (Figure 2). Models have a spread in diurnal amplitude  
46 227 and phase, with precipitation amplitudes ranging from 1.5 to 6 mm/day and the diurnal phases  
47 228 occurring as early as 12 LST to as late as 17 LST. The diurnal phases in both observations and  
48 229 models are more similar in the dry season than in the wet season, while the precipitation amounts  
49 230 and amplitudes are larger in the wet season for observation and most models (Figure 2). Since  
50 231 DCP is affected by several types of convective systems that occur at different times of the day in  
51 232 both dry and wet seasons (e.g., Tang et al. 2016), we will focus on model performance for  
52 233 different types of convective systems instead of in different seasons.

53  
54  
55  
56  
57  
58  
59  
60

1  
2  
3 234 The observed cloud fractions at SGP and MAO both show a low-level cloud peak rising along  
4 235 with the daytime boundary layer development (Figure 3). The transition of shallow-to-deep  
5 236 convection has been extensively studied focusing on the following mechanisms: boundary layer  
6 237 turbulence strength, including boundary layer inhomogeneity (e.g., Zhang and Klein 2010) and  
7 238 cold pools from rain evaporation (e.g., Khairoutdinov and Randall 2006; Mapes and Neale 2011;  
8 239 Del Genio et al. 2012); and free troposphere humidity and instability, including the  
9 240 preconditioning from shallow convection via detrainment or dilution (e.g., Rio et al. 2009;  
10 241 Mapes and Neale 2011; Del Genio et al. 2012; de Rooy et al. 2013; Hohenegger and Stevens  
11 242 2013; Ruppert and Johnson 2015; Zermeño-Díaz et al. 2015). Most of these studies used  
12 243 observations or idealized models, and only a few of them attempted to represent the transition in  
13 244 GCMs (e.g., Rio et al. 2009; Del Genio et al. 2012). Among the eight SCMs, SAM0-UNICON  
14 245 well captures the gradually rising of low clouds peak at both SGP and MAO; EAMv1 and  
15 246 SCAM6 capture the low clouds rising, although their low cloud fraction is underestimated at  
16 247 SGP; other models all fail to produce the rising low clouds in the daytime. This result reveals the  
17 248 importance of unifying turbulence and shallow convective scheme (CLUBB) or shallow and  
18 249 deep convective scheme (UNICON) in simulating the development of shallow clouds and the  
19 250 transition from shallow to deep clouds. This is consistent with the findings in previous attempts  
20 251 of unified schemes such as in Frenkel et al. (2011a, 2011b), which used a simple multcloud  
21 252 model coupled to a bulk boundary layer scheme to simulate the diurnal cycle of tropical  
22 253 precipitation. For high clouds, most models overestimate high cloud fraction comparing to  
23 254 observations at SGP and MAO. The diurnal variation of high clouds is also poorly simulated at  
24 255 SGP but reasonably reproduced at MAO. The different model performances in different  
25 256 locations indicate the complexity to develop globally uniform parameterizations.

26  
27  
28 257 Previous studies have shown a relationship between precipitation and column-integrated relative  
29 258 humidity (CRH) in observations at daily (e.g., Bretherton et al. 2004) and sub-daily (e.g.,  
30 259 Holloway and Neelin 2009; Neelin et al. 2009) timescales, although it should be noted that using  
31 260 CRH is an approximation for a more complex precipitation-moisture-temperature relationship  
32 261 (Kuo et al. 2018). How well models can capture the observed precipitation-CRH relationship is  
33 262 related to the representation of convection and its interaction with the large-scale environment  
34 263 and provides insights to model improvements on convection and precipitation (e.g., Kuo et al.  
35 264 2020). Here we also examine the relationship of precipitation amount and frequency with CRH,  
36 265 as well as the occurrence frequency of each CRH bin (2% interval) in Figure 4. Observations  
37 266 show a strongly increasing relationship between precipitation amount and CRH at both sites.  
38 267 Precipitation picks up quickly and increases exponentially when CRH reaches 60% ~ 70% at  
39 268 SGP and 75% ~ 80% at MAO. Most models, except ICON, simulate higher (lower) precipitation  
40 269 probability (Figure 4 mid-row) and precipitation amount (Figure 4 top-row) compared to the  
41 270 observations when CRH is low (high). However, there are also more high-CRH days and less  
42 271 moderate-CRH days in these models than in observations (Figure 4 bottom-row). This indicates  
43 272 that models tend to produce light rainfall too easily in moderately dry conditions but have  
44 273 difficulties producing strong precipitation in wet conditions, although they are more likely to

1  
2  
3 274 produce high CRH. This is consistent with the long-standing model error in GCMs that models  
4 275 rain too frequently at reduced intensity (Dai 2006; Sun et al. 2007; Stephens et al. 2010). In  
5 276 ICON, precipitation picks up at a much higher CRH. It also produces more wet conditions and  
6 277 less dry conditions than observations and other models. This may be related to the fact that  
7 278 ICON requires the whole box to be saturated for large-scale precipitation while other models  
8 279 allow partial cloudiness for microphysics. This would lead to a later onset of large-scale  
9 280 precipitation and higher relative humidity in ICON.

13 281 In the next two subsections, we select two convection regimes to further investigate the model  
14 282 biases on DCP: afternoon precipitation regime that is primarily surface-driven deep convection  
15 283 and nocturnal precipitation regime that is primarily associated with propagating MCSs and  
16 284 elevated convection. Based on observations, the afternoon precipitation days are selected by  
17 285 modifying the criteria of Zhang and Klein (2010). For SGP, an afternoon precipitation day is  
18 286 chosen when it has (1) peak rain rate greater than 1 mm/day, (2) rain peak time between 13 and  
19 287 20 LST and (3) the peak rain rate 1.5 times greater than any rain rate outside of 13 to 20 LST.  
20 288 For MAO, an afternoon precipitation day is chosen when it has (1) peak rain rate greater than 1  
21 289 mm/day, (2) rain peak time between 11 and 20 LST, (3) the peak rain rate 1.5 times greater than  
22 290 any rain rate outside of 11 to 20 LST, and (4) it must fall into the locally-driven convection case  
23 291 library visually selected from radar and satellite images (Tian et al. 2021). The last criterion is set  
24 292 to exclude those cases of propagating MCSs with a daytime rainfall peak, which occur frequently  
25 293 during the rainy season at MAO and overlap with locally generated rainfall (Tang et al. 2016). A  
26 294 nocturnal precipitation day at SGP and MAO is chosen when it has (1) peak rain rate greater than  
27 295 1 mm/day, and (2) rain peak time between 00 and 07 LST. Overall, there are 136 and 380 days  
28 296 selected for the afternoon and nocturnal precipitation days, respectively, during the twelve warm  
29 297 seasons at SGP, and 111 and 73 days selected for the afternoon and nocturnal precipitation days,  
30 298 respectively, during the two years at MAO.

### 37 38 299 3.2 Afternoon Precipitation Regime

40 300 The mean diurnal cycle of total precipitation and convective precipitation fraction for the  
41 301 selected afternoon precipitation days at SGP and MAO are shown in Figure 5. Also shown are  
42 302 the harmonic dial plots of total precipitation. The observations show that the afternoon regime  
43 303 precipitation picks up after 09 LST at both sites, reaches a daily maximum around 17 LST at  
44 304 SGP and 14 LST at MAO, then decreases to late-night/early-morning values around 21 LST. In  
45 305 the diurnal harmonic analysis, the diurnal phase of afternoon precipitation at SGP is well  
46 306 captured in most SCMs, as opposed to the timeseries of all events in Figure 1, while their diurnal  
47 307 amplitudes vary. At MAO, models have a large spread of afternoon precipitation peak time,  
48 308 consistent with the timeseries of all events in Figure 1. EAMv1 shows large precipitation in the  
49 309 morning with the diurnal phase peak at noon; SMCP and SAM0-UNICON have a late  
50 310 afternoon peak just after 18 LST; SCAM6, SKIM and TaiESM1 capture the observed diurnal  
51 311 phase, but their diurnal amplitudes are much smaller. ICON produces two precipitation peaks,  
52 312 one in the morning and the other in the late afternoon, with much lower magnitude. The different  
53  
54  
55  
56  
57  
58  
59  
60

1  
2  
3 313 model treatments of the preconditioning, triggering, developing of convection and convection  
4 314 interaction with environment via entrainment/detrainment may be responsible for the large  
5 315 spread or model performance. Another aspect is the presence of cold pool environments and  
6 316 associated boundary layer features and triggering of secondary developments, leading to the  
7 317 propagation as well as organization of convection (e.g., Oliveira et al. 2020). It is also likely that  
8 318 these processes are complex and location-dependent, so that effort is needed to improve the  
9 319 current globally uniform convective parameterization.

13 320 Figure 6 shows the frequency of diurnal maximum precipitation occurrence at each hour. The  
14 321 model performance of maximum precipitation frequency is consistent with their performance of  
15 322 mean DCP in Figure 5. The maximum diurnal precipitation occurs mostly between 15 – 19 LST  
16 323 at SGP and 13 – 17 LST at MAO, consistent with the time of large mean diurnal precipitation  
17 324 (Figure 5). Models generally capture the maximum precipitation time at SGP, with a few  
18 325 percentages of time when models produce maximum precipitation too early or too late. At MAO,  
19 326 models frequently produce maximum precipitation either too early or too late compared to  
20 327 observation, except SKIM. This again indicates that the response of model precipitation to  
21 328 environment at moist tropical land is not as sophisticated as at mid-latitude land.

26 329 In the daytime, all models produce most of their precipitation from convection, with convective  
27 330 precipitation fraction close to 100% (second row of Figure 5). The model performance of  
28 331 afternoon convection is further examined by looking at the vertical profiles of apparent heating  
29 332 ( $Q_1$ ) and drying ( $Q_2$ ) in Figure 7.  $Q_1$  and  $Q_2$  were first introduced by Yanai et al. (1973) to  
30 333 estimate the diabatic processes:

34 334 
$$Q_1 = \frac{1}{c_p} \left( \frac{\partial \bar{s}}{\partial t} + \bar{\vec{V}} \cdot \nabla \bar{s} + \bar{\omega} \frac{\partial \bar{s}}{\partial p} \right) = \frac{1}{c_p} \left( Q_{rad} + L_v(d_w + d_i) - \frac{\partial \overline{\omega' s'}}{\partial p} \right) \quad (1)$$

37 335 
$$Q_2 = -\frac{L_v}{c_p} \left( \frac{\partial \bar{q}}{\partial t} + \bar{\vec{V}} \cdot \nabla \bar{q} + \bar{\omega} \frac{\partial \bar{q}}{\partial p} \right) = \frac{L_v}{c_p} \left( d_w + d_i + \frac{\partial \overline{\omega' q'}}{\partial p} \right) \quad (2)$$

39 336 where  $s = C_p T + gz$  is the dry static energy and  $C_p$  is the specific heat for dry air in constant  
40 337 pressure;  $q$  is water vapor mixing ratio;  $\vec{V}$  is horizontal wind vector;  $\omega$  is vertical velocity in  
41 338 pressure coordinate;  $Q_{rad}$  is radiative heating;  $L_v(d_w + d_i)$  is the latent heat from liquid and ice  
42 339 processes; the overbar refers to a horizontal average and the prime refers to a deviation from the  
43 340 average. The “observed”  $Q_1$  and  $Q_2$  are derived from the large-scale dynamics (the center part of  
44 341 the equations) from the variational analysis while the “simulated”  $Q_1$  and  $Q_2$  are the sum of all  
45 342 physical tendencies in the model (the right-hand-side of the equations). The simulated vertical  
46 343 profiles of  $Q_1$  and  $Q_2$  are generally consistent with observations at SGP (Figure 7, left column),  
47 344 with heating peak in the middle to upper troposphere around 400 to 500 hPa. However, there are  
48 345 large discrepancies of  $Q_1$  and  $Q_2$  profiles at MAO (Figure 7, right column). Models produce a  
49 346 heating peak near 700 to 800 hPa, much lower than the observed peak at near 500 hPa. While the  
50 347 observed heating remains large to about 150 mb, model heating is small about 500 mb. They also  
51 348 fail to reproduce the observed moisture sink between 250 and 650 hPa. These discrepancies were

1  
2  
3 349 also found in Large Scale Biosphere–Atmosphere Experiment (LBA) conducted in Southwest  
4 350 Amazonia (Ma et al. 2021a), indicating that models produce too shallow afternoon convection  
5  
6 351 over the broad Amazon region. The fact that models simulate  $Q_1$  and  $Q_2$  well at SGP but poorly  
7 352 at MAO also highlights the dependence of model performances at different locations. The poor  
8  
9 353 performance at deep convection at MAO despite being driven by observed large-scale forcing  
10 354 suggests significant common deficiencies in deep convective parameterization over tropical land.

11  
12 355 At both SGP and MAO, a common model bias in DCP is the early onset of precipitation. The  
13 356 observed diurnal precipitation at both SGP and MAO picks up quickly near 12 LST, while many  
14 357 models produce notable precipitation a few hours earlier (Figure 5). To further quantify the early  
15 358 onset of precipitation, we define the precipitation onset time as the first hour after 06 LST when  
16 359 the precipitation at that hour increases above 1 mm/day. The statistics of precipitation onset time  
17 360 are shown in Figure 8. The models we are discussing in this section are shown in thick lines, and  
18 361 those will be discussed in Section 4 for sensitivity study are shown in thin lines. The mean onset  
19 362 time of precipitation is observed in early afternoon at SGP and around noon at MAO, about 3–4  
20 363 hours earlier than the maximum precipitation time (Figure 6). However, the SCM-simulated  
21 364 onset time is usually 1 to 2 hours earlier than in observations at SGP, and up to 4 hours earlier at  
22 365 MAO, even for those models produce maximum precipitation in a later time (Figure 6). CMC  
23 366 and ICON have a consistent mean precipitation onset time with observation at MAO, but their  
24 367 diurnal distribution is broader, with three (CMC) or two (ICON) precipitation peaks during the  
25 368 daytime (top right panel of Figure 5).

26  
27  
28  
29  
30  
31 369 Among these SCMs, EAMv1, SCAM6, SMCPCP and ICON use CAPE to trigger deep  
32 370 convection (Table 2). This CAPE-based convective trigger is believed to trigger convection too  
33 371 easily and too frequently (e.g., Xie and Zhang 2000; Ma et al. 2021b). A modified trigger using  
34 372 dynamic CAPE (dCAPE) introduced by Xie and Zhang (2000) and further enhanced in Xie et al.  
35 373 (2019) is implemented in EAMv1. trigger and show promising results on mitigating the early  
36 374 onset of convection (see further discussion in Section 4). Using a CIN-based convective trigger,  
37 375 SKIM shows good precipitation onset time at SGP, but too early onset time at MAO, possibly  
38 376 due to the low-CIN environment in the Amazon permitting convection to trigger too easily but  
39 377 not through a sufficient deep layer.

40  
41  
42  
43  
44 378 Another well-known issue of early onset of deep convection in GCMs is the poor simulation of  
45 379 the transition of shallow-to-deep convection and the gradual moistening of the free troposphere  
46 380 (Guichard et al. 2004; Zhang and Klein 2010). Shallow and deep convection is usually related to  
47 381 very different forcing regimes, entrainment and detrainment rates, and environment conditions.  
48 382 Therefore, almost all previous GCMs separate them into different schemes, and they work  
49 383 reasonably well in practice. However, separating the two schemes usually leads to an overly  
50 384 abrupt transition from one condition to another (e.g., Rio et al. 2009). Deep convection is often  
51 385 triggered as soon as the large-scale environment reaches the triggering criterion in the model,  
52 386 instead of developing through an intermittent stage of preconditioning of the free atmosphere as  
53 387 in the real world. SAM0-UNICON uses a new parameterization that aims to unify shallow and  
54  
55  
56  
57  
58  
59  
60

1  
2  
3 388 deep convective schemes to simulate the complex interactions between subgrid and grid-scale  
4 389 processes such as the transition from shallow to deep convection. While it correctly simulates the  
5 390 precipitation onset time at SGP, at MAO in encounters similar deficiency of ~2 hr earlier onset  
6 391 time (Figure 8). It may be partly related with the inability of SCM to handle horizontal advection  
7 392 of subgrid cold pool that is parameterized within UNICON. This reveals a major challenge in  
8 393 unified parameterization to treat all conditions within a single set of equations and a need to test  
9 394 the models in global simulations.

### 13 395 3.3 Nocturnal Precipitation Regime

15 396 The mean diurnal cycle of total precipitation, convective precipitation fraction and the diurnal  
16 397 harmonic dial plots of total precipitation for nocturnal precipitation days are shown in Figure 9.  
17 398 Nocturnal precipitation is typically related to the elevated convection above nocturnal stable  
18 399 boundary layer (e.g., Lee et al. 2008; Geerts et al. 2017) or propagating MCSs. The observations  
19 400 show a diurnal peak at ~03 LST at SGP and ~05 LST at MAO, with a diurnal peak of ~20  
20 401 mm/day and harmonic amplitude of ~8 mm/day, much larger than the afternoon precipitation  
21 402 events in Figure 5. At 12~15 LST, precipitation at SGP reaches its diurnal minimum, while  
22 403 precipitation at MAO reaches a secondary peak, close to but, weaker than the peak of afternoon  
23 404 precipitation. This indicates that even when the nocturnal precipitation has released some  
24 405 instability of the atmosphere, the solar heating in the following daytime and the moist  
25 406 environment can still trigger afternoon convection.

26 407 From Figure 9, SCMs can be divided into two groups in simulating nocturnal precipitation at  
27 408 SGP. SKIM, CMC and TaiESM1 well capture the diurnal phase and amplitude of nocturnal  
28 409 precipitation, and ICON also captures the diurnal phase but underestimates the amplitude of  
29 410 nocturnal precipitation. EAMv1, SCAM6, SAM0-UNICON and SMPCPCP produce diurnal  
30 411 precipitation later with smaller magnitude. At MAO, the four “good” models also perform well,  
31 412 while the other models produce either a smaller magnitude or later phase of DCP. Between 00  
32 413 and 06 LST, SKIM, CMC, TaiESM1 and ICON produce most of their precipitation (70% – 90%)  
33 414 from the convective parameterization at both sites, while other models produce ~60% of their  
34 415 precipitation at SGP and 40% – 95% of their precipitation at MAO as large-scale precipitation.  
35 416 Although impacted by convective process such as latent heating and detrainment, the large-scale  
36 417 precipitation produced in SCMs is primarily attributed to the prescribed large-scale forcing,  
37 418 which is constrained by the observed surface precipitation. In free-run GCMs, where the large-  
38 419 scale forcing interacts with model physics and is affected by their deficiencies, the simulation of  
39 420 nocturnal precipitation could be even worse (e.g., Tang et al. 2021). Thus, it seems to be  
40 421 necessary to improve the deficiencies in model parameterizations found in the present study. that  
41 422 might potentially contribute to model errors in a less constrained model setup.

42 423 There is a distinguishing feature that separates these two groups of models: whether or not the  
43 424 model allows elevated convection triggered above the boundary layer. EAMv1, SCAM6 and  
44 425 SMPCPCP all use the ZM deep convective scheme with the launching parcel chosen only within

1  
2  
3  
4  
5  
6  
7  
8  
9  
10  
11  
12  
13  
14  
15  
16  
17  
18  
19  
20  
21  
22  
23  
24  
25  
26  
27  
28  
29  
30  
31  
32  
33  
34  
35  
36  
37  
38  
39  
40  
41  
42  
43  
44  
45  
46  
47  
48  
49  
50  
51  
52  
53  
54  
55  
56  
57  
58  
59  
60

1  
2  
3 426 the boundary layer. SKIM and TaiESM1 select air parcels below  $\sim 700$  hPa ( $\sigma=0.7$ ) and 600 hPa,  
4 427 respectively, and ICON selects air parcels within 350hPa above the surface. It is natural to  
5  
6 428 hypothesize that allowing convection to occur above the boundary layer is the key to simulate  
7 429 nocturnal convection. In the sensitivity study in Section 4, when the default ZM scheme is  
8  
9 430 modified by unlimiting the launching level, the nocturnal precipitation in EAMv1.trigger is  
10 431 significantly improved compared to default EAMv1. CMC has a separated mid-level convective  
11 432 scheme to capture elevated convection (McTaggart-Cowan et al. 2020). The mid-level scheme  
12 433 exhibits a maximum activity during the night (Figure 10). However, its contribution to the total  
13 434 precipitation is very modest while deep convection contributes the most for nocturnal  
14 435 precipitation. Further sensitivity tests with different thresholds for deep and mid-level convection  
15 436 triggering have shown little sensitivity of the phase of DCP to how active the deep and mid-level  
16 437 schemes are.

19  
20 438 Figure 11 shows the 00-06 LST mean vertical profiles of  $Q_1$  and  $Q_2$  at SGP and MAO for the  
21 439 nocturnal precipitation events. The observed heating profile is top-heavy at SGP and roughly  
22 440 parabolic at MAO, showing typical convective conditions over mid-latitude continent and  
23 441 tropics, respectively. The condensational drying has a sharper and stronger peak at MAO than  
24 442 SGP. It is interesting to see that all models produce heating and drying peaks at a similar height  
25 443 to that of the observed, despite their wide ranges of convective fraction as shown in Figures 5  
26 444 and 9 (e.g., Schumacher et al. 2004). The reasonable simulation of nocturnal convective heating  
27 445 depth at MAO (Figure 11b) is notable given the poor performance at afternoon convective  
28 446 heating depth (Figure 7b), possibly related to that, afternoon convection is locally-driven while  
29 447 nocturnal convection is propagating organized convection. The magnitude of  $Q_1$  and  $Q_2$  varies  
30 448 among models. SKIM, TaiESM1 and CMC produce similar magnitudes of  $Q_1$  and  $Q_2$   
31 449 comparable with observations, while the other models produce smaller magnitudes (except  
32 450 ICON  $Q_1$  at MAO). The reduction of the  $Q_1$  peak in these models is more prevalent in the upper  
33 451 levels, which may be related to the weaker convective activity that is not sufficient to remove all  
34 452 the instability from the large-scale forcing. The remaining instability in these models is then  
35 453 released at a later time, causing the morning-time precipitation peak seen in Figure 9.

41  
42 454

#### 43 44 455 **4. Sensitivity Study**

45  
46 456 In addition to the default simulations, some modeling centres also performed other simulations  
47 457 using different model versions, physical schemes or configurations. Table 3 shows the  
48 458 information of the simulations included in this section emphasizing their differences from the  
49 459 default models/runs. DCP in SKIM.nudge is very similar to the default runs, so we choose not to  
50 460 show them to make the figures more readable. Moreover, SAM0-UNICON is included in this  
51 461 sensitivity study because of two reasons: firstly, it is developed from SCAM5, with the same  
52 462 turbulence, microphysics and macrophysics schemes but a different convective scheme;

53  
54  
55  
56  
57  
58  
59  
60

1  
2  
3 463 secondly, it unifies shallow and deep convection, so we feel it is interesting to compare it with  
4 464 another model with unified shallow and deep convection (EAMv1.SILHS).

6  
7 465 Figure 12 shows DCP performance of the models for sensitivity study in the afternoon  
8 466 precipitation regime, while Figure 13 shows DCP performance in the nocturnal precipitation  
9 467 regime. EAMv1.trigger uses a modified convective trigger, which uses a dynamic CAPE  
10 468 (dCAPE: CAPE changes due to large-scale advectons) to trigger convection and allow air  
11 469 parcels to launch above the boundary layer. The improvement of DCP in GCMs has been  
12 470 demonstrated in Xie et al. (2019), Wang et al. (2020) and (Cui et al. 2021). Here for SCM, the  
13 471 improvement of DCP is also shown at SGP and MAO (Figures 12 and 13) (blue dashed line and  
14 472 open circle). We believe that the dCAPE trigger helps delay the precipitation onset of afternoon  
15 473 precipitation while allowing air parcels to launch above the boundary layer helps convection  
16 474 occur at night.

20  
21 475 Another independent modification of EAMv1, EAMv1.SILHS, also shows significant  
22 476 improvement on DCP in the two precipitation regimes. Instead of using ZM for deep convection  
23 477 and CLUBB for shallow convection and large-scale clouds and precipitation in the default  
24 478 EAMv1, EAMv1.SILHS uses CLUBB for all shallow convection, deep convection and large-  
25 479 scale clouds and precipitation. Therefore, the convective fraction is zero because it does not  
26 480 separate convective and large-scale precipitation. The CLUBB is interfaced to the microphysics  
27 481 scheme using the subgrid sampler SILHS. It well captures the elevated convection at night as  
28 482 shown in Figure 13, possibly because it does not need a convective trigger nor specification of  
29 483 parcel launching level. For afternoon precipitation, it delays the precipitation onset time on both  
30 484 SGP and MAO (Figure 8), but only produces about half of the observed peak precipitation and  
31 485 ~30% of the harmonic amplitude (Figure 12). This is subject to further improvements.

35  
36 486 Another model with a unified convective scheme, SAM0-UNICON, is also shown in Figures 12  
37 487 and 13. Note that SAM0-UNICON and SCAM6 both have a tight relationship with SCAM5:  
38 488 SAM0-UNICON has the same turbulence, microphysics and macrophysics schemes as SCAM5,  
39 489 but a different shallow and deep convective scheme. SCAM6 only shares the same deep  
40 490 convective scheme with SCAM5, with turbulence, shallow convection and macrophysics  
41 491 replaced by CLUBB. The DCP performance in SCAM6 is similar as in SCAM5, while SAM0-  
42 492 UNICON shows larger differences with SCAM5. This indicates that DCP is primarily controlled  
43 493 by the deep convective scheme. Since SAM0-UNICON can simulate the complex interactions  
44 494 between subgrid and grid-scale processes such as the transition from shallow to deep convection,  
45 495 it captures well the afternoon precipitation, especially at SGP. However, its performance on  
46 496 nighttime precipitation still needs to be improved. This is consistent with previous work in global  
47 497 simulations (Park 2014b; Tang et al. 2021).

52  
53 498 Two models conducted sensitivity tests with an interactive land model. SCAM6 is coupled with  
54 499 the community land model version 5.0 (CLM5, Lawrence et al. 2019), while SKIM is coupled  
55 500 with the revised Noah land surface model version 3.4.1 (Koo et al. 2017). SKIM.land performs  
56  
57  
58  
59  
60

1  
2  
3 501 similar to the default SKIM run, while SCAM6.land performs better than SCAM6, with the early  
4 502 onset of afternoon precipitation (see Figure 8 and Figure 12) and the morning rainfall in  
5 503 nocturnal precipitation days (Figure 13) both reduced. It is interesting to see that SCAM6.land  
6 504 produces much lower latent heat fluxes and higher sensible heat fluxes than observations (Figure  
7 505 14). The estimated ground heat flux is also much larger in SCAM6.land than in other models,  
8 506 with daily mean of  $61.7 \text{ W/m}^2$  at SGP and  $59.0 \text{ W/m}^2$  at MAO. The corresponding ground heat  
9 507 flux in SCAM6 is  $-9.4 \text{ W/m}^2$  at SGP and  $-3.9 \text{ W/m}^2$  at MAO, and that in the observations is  
10 508  $4.9 \text{ W/m}^2$  at SGP and  $-5.3 \text{ W/m}^2$  at MAO. On the other hand, SKIM.land also produces lower  
11 509 latent heat fluxes and higher sensible heat fluxes than observations, likely due to more humid  
12 510 near-surface air or misrepresented surface conditions such as vegetation fraction, land type or  
13 511 soil properties. Its turbulent flux errors are smaller than SCAM6.land, and its ground heat flux is  
14 512 similar with SKIM and observations. Despite the differences in the land models used in  
15 513 SCAM6.land and SKIM.land, it may be inferred that the land-atmospheric interactions in climate  
16 514 models are not well represented so that a model (SCAM6.land) needs to produce more  
17 515 unrealistic surface fluxes in order to get more realistic precipitation in deep convective regimes.  
18  
19  
20  
21  
22  
23  
24 516

## 25 26 517 **5. Summary and Discussions**

27  
28 518 The diurnal cycle of precipitation (DCP) is a problem that GCMs have struggled to represent in  
29 519 past decades (Fiedler et al. 2020). Although the latest GCMs in the recent CMIP6 have shown  
30 520 improvement in simulating DCP (Tang et al. 2021), they still suffer from the persistent problems  
31 521 of too early precipitation and missing nocturnal precipitation.  
32  
33

34 522 The GEWEX Global Atmospheric System Study (GASS) Panel organized a project focusing on  
35 523 understanding and improving the model capability to simulate diurnal precipitation phenomena  
36 524 through multi-model intercomparison studies against observations. This study focuses on the  
37 525 intercomparison of SCMs to understand what processes control the diurnal cycle of precipitation  
38 526 over different climate regimes and identify the deficiencies and missing physics in current model  
39 527 parameterizations. Instead of focusing on a particular intensive observing period for several days  
40 528 to a few months as in previous SCM intercomparison studies, we have performed long-term  
41 529 hindcast simulations to obtain robust statistics of model performances on DCP. Eleven SCMs  
42 530 from different modeling centers around the world have participated in this project.  
43  
44  
45  
46

47 531 DCP in twelve summer seasons at a midlatitude land site (SGP) and two continuous years at a  
48 532 tropical land site (MAO) are investigated in this study. The two selected sites have distinguished  
49 533 and representative characteristics of the large-scale environment, clouds and precipitation. The  
50 534 participating SCMs do not always show the same discrepancies at the two sites. This indicates  
51 535 that some parameterization assumptions may not work well across all climate regimes.  
52  
53

54 536 Two regimes of DCP are examined in this study, one is surface-driven afternoon convection and  
55 537 the other is nocturnal precipitation caused by elevated convection or propagating convective  
56  
57  
58  
59  
60

1  
2  
3 538 systems. For afternoon convection, precipitation in most SCMs initiated 1 to 4 hours earlier than  
4 539 observation. The early onset of precipitation is more severe at MAO than at SGP. It appears to be  
5 540 associated with two other issues common across all the models for MAO afternoon precipitation  
6 541 cases: a severe deficiency of convective heating in the upper troposphere, and rainfall too evenly  
7 542 spread across times of day. In other words for the MAO afternoon cases, models fail to develop  
8 543 strong deep convection but precipitate too easily from convection in the lower troposphere. At  
9 544 SGP, the early onset of afternoon precipitation may be due to the missing transition of shallow-  
10 545 to-deep convection in climate models. More sophisticated parameterizations that unify shallow  
11 546 and deep convection (e.g., UNICON, CLUBB-SILHS) can improve the early onset problem,  
12 547 although UNICON shows more deficiencies in the precipitation-CRH relationship. For nocturnal  
13 548 precipitation, although all SCMs produce considerable precipitation at night, the partitioning of  
14 549 convective precipitation and large-scale precipitation differ dramatically among models. Models  
15 550 with most of the nocturnal precipitation generated from large-scale are likely driven by the  
16 551 prescribed large-scale forcing. SCMs that produce most of nocturnal precipitation from  
17 552 convection (SKIM, TaiESM1, CMC, ICON and EAMv1.trigger) all allow convection to be  
18 553 triggered above the boundary layer. Although a few recent studies have considered convection  
19 554 moving across grids (Malardel and Bechtold 2019; McTaggart-Cowan et al. 2019b), most SCMs  
20 555 and their parent GCMs still struggle to propagate convection from one grid to another. The  
21 556 capability to detect mid-level instability above the boundary layer is important for them to  
22 557 simulate nocturnal precipitation.

23 558 Sensitivity studies were performed using continuous nudging runs, different parameterizations,  
24 559 or interactive land models. Using a revised convective trigger specifically targeting improvement  
25 560 on the diurnal cycle of precipitation, EAMv1.trigger shows the importance of dynamically  
26 561 constraining the convective trigger and allowing parcels to launch above the boundary layer in  
27 562 traditional convective parameterizations to produce precipitation at the right time. Another path  
28 563 towards improving DCP is the effort of unifying shallow and deep convection, as seen in SAM0-  
29 564 UNICON and EAMv1.SILHS. On the other hand, in the two land-atmosphere coupled  
30 565 simulations, the one with larger biases in surface turbulent fluxes (SCAM6.land) shows more  
31 566 improvement on DCP. This indicates that the relationship between the land-atmospheric  
32 567 interaction and DCP is complicated and points to the importance of the representation of  
33 568 boundary-layer processes in deep convective regimes. Further study is needed to investigate how  
34 569 the representation of land-atmospheric coupling will influence simulation of DCP.

35 570 Although not the focus of this study here, the discrepancy in the amplitude of DCP should also  
36 571 be pointed out. In addition to deep and shallow convection, boundary layer processes can highly  
37 572 contribute to the control of the diurnal amplitude (e.g., Koo and Hong 2010). Therefore, a  
38 573 diversity of turbulence schemes (Table 1) might be a source of large spread in diurnal amplitude,  
39 574 which needs to be addressed in future study.

40 575 This SCM intercomparison study provides insights of which physical processes are essential in  
41 576 climate models to simulate DCP, given a large-scale environment close to the real world. In a  
42  
43  
44  
45  
46  
47  
48  
49  
50  
51  
52  
53  
54  
55  
56  
57  
58  
59  
60

1  
2  
3 577 global or regional model, the model biases in large-scale dynamic and thermodynamic states and  
4 578 the interactions between the large-scale fields and physics also impact the simulation of DCP.  
5  
6 579 This is not revealed in the SCM study. An intercomparison of global and regional climate models  
7 580 is currently underway and more details will be presented on DCP over broader regions in the  
8 581 near future.  
9

10  
11 582

12  
13 583 *Acknowledgement:*

14  
15 584 *This work is part of The GEWEX Global Atmospheric System Study (GASS) Panel's Diurnal*  
16 585 *Cycle of Precipitation Project. Work at LLNL is supported by the Earth and Environmental*  
17 586 *System Modeling, Regional and Global Model Analysis, Atmospheric System Research and*  
18 587 *Atmospheric Radiation Measurement programs, funded by the U.S. Department of Energy,*  
19 588 *Office of Science, Office of Biological and Environmental Research, and performed under the*  
20 589 *auspices of the U.S. DOE by Lawrence Livermore National Laboratory under Contract DE-*  
21 590 *AC52-07NA27344. S. Tang was partially supported by the "Enabling Aerosol-cloud interactions*  
22 591 *at GLocal convection-permitting scales (EAGLES)" project (74358) funded by the U.S.*  
23 592 *Department of Energy, Office of Science, Office of Biological and Environmental Research,*  
24 593 *Earth System Model Development program. Pacific Northwest National Laboratory (PNNL) is*  
25 594 *operated for DOE by Battelle Memorial Institute under contract DE-AC05-76RL01830. J. D.*  
26 595 *Neelin was supported by NSF project AGS-1936810.*  
27  
28  
29 596  
30  
31  
32  
33  
34  
35  
36  
37  
38  
39  
40  
41  
42  
43  
44  
45  
46  
47  
48  
49  
50  
51  
52  
53  
54  
55  
56  
57  
58  
59  
60

1  
2  
3 **597 Appendix: Model schemes and abbreviations in Tables 1, 2 and 3**  
4

5 598 Bechtold14: convective scheme from Bechtold et al. (2014)  
6 599 CAPE: convective available potential energy  
7 600 CIN: convective inhibition  
8 601 CLUBB: Cloud Layers Unified By Binormals (Golaz et al. 2002; Larson and Golaz 2005; Larson 2017)  
9 602 dCAPE: dynamic CAPE generation rate from large-scale tendency (Xie and Zhang 2000)  
10 603 UW-diag\_TKE: University of Washington diagnostic turbulent kinetic energy scheme (Bretherton and  
11 604 Park 2009)  
12 605 GTS: Global Forecast System (GFS) – Taiwan Earth System Model (TaiESM) – Sundqvist scheme (Shiu  
13 606 et al. 2021)  
14 607 HanPan: shallow convection from Han and Pan (2011)  
15 608 HB: turbulent scheme from Holtslag and Boville (1993)  
16 609 Köhler20: cloud cover parameterization from Köhler (2020)  
17 610 KSAS: Korean Integrated Model (KIM, Hong et al. 2018) version of the simplified Arakawa-Schubert  
18 611 deep convection scheme (Han et al. 2020)  
19 612 LCL: lifting condensation level  
20 613 LFC: level of free convection  
21 614 M-Bechtold: modified from Bechtold et al. (2001) (McTaggart-Cowan et al. 2019a)  
22 615 MG: bulk two-moment cloud microphysics (Morrison and Gettelman 2008)  
23 616 MG2: version 2 of MG microphysics (Gettelman et al. 2015)  
24 617 Modified KF: modified from Kain and Fritsch (1990) (McTaggart-Cowan et al. 2019a)  
25 618 Park1: macrophysics from (Park et al. 2014)  
26 619 Park2: macrophysics from (Park et al. 2017)  
27 620 PCH16: macrophysics from (Park et al. 2016)  
28 621 UW-PB09: University of Washington shallow convective scheme (Park and Bretherton 2009)  
29 622 PBL: planetary boundary layer  
30 623 Raschendorfer00: turbulence scheme from Raschendorfer (2000)  
31 624 Seifert08: single moment microphysics from Seifert (2008)  
32 625 Shin-Hong: turbulence scheme from Shin and Hong (2015) with revision of Lee et al. (2018)  
33 626 SILHS: Subgrid Importance Latin Hypercube Sampler (Thayer-Calder et al. 2015; Griffin and Larson  
34 627 2016)  
35 628 Sundqvist: microphysics from Sundqvist et al. (1989)  
36 629 TKE1.5: 1.5 order turbulent kinetic energy scheme from McTaggart-Cowan et al. (2019a)  
37 630 UNICON: Unified convective scheme (Park 2014a, 2014b)  
38 631 Unified stochastic Plume-ZM: Unified Stochastic Mass-flux Cumulus integrated in ZM scheme  
39 632 (Khouider and Leclerc 2019)  
40 633 WSM5: the Weather Research and Forecasting (WRF) single-moment 5-class microphysics scheme  
41 634 (Hong et al. 2004; Bae et al. 2016; Kim and Hong 2018)  
42 635 ZM: Zhang-McFarlane convective scheme (Zhang and McFarlane 1995)  
43 636  
44  
45  
46  
47  
48  
49  
50  
51  
52  
53  
54  
55  
56  
57  
58  
59  
60

637

## 638 References:

- 639 Bae, S. Y., S.-Y. Hong, and K.-S. S. Lim, 2016: Coupling WRF Double-Moment 6-Class Microphysics  
640 Schemes to RRTMG Radiation Scheme in Weather Research Forecasting Model. *Advances in*  
641 *Meteorology*, **2016**, 5070154, 10.1155/2016/5070154.
- 642 Bašták Ďurán, I., and Coauthors, 2021: The ICON Single-Column Mode. *Atmosphere*, **12**, 906.
- 643 Bechtold, P., and Coauthors, 2000: A GCSS model intercomparison for a tropical squall line observed  
644 during toga-coare. II: Intercomparison of single-column models and a cloud-resolving model. *Quarterly*  
645 *Journal of the Royal Meteorological Society*, **126**, 865-888, 10.1002/qj.49712656405.
- 646 Bechtold, P., E. Bazile, F. Guichard, P. Mascart, and E. Richard, 2001: A mass-flux convection scheme  
647 for regional and global models. *Quarterly Journal of the Royal Meteorological Society*, **127**, 869-886,  
648 <https://doi.org/10.1002/qj.49712757309>.
- 649 Bechtold, P., J.-P. Chaboureau, A. Beljaars, A. K. Betts, M. Köhler, M. Miller, and J.-L. Redelsperger,  
650 2004: The simulation of the diurnal cycle of convective precipitation over land in a global model.  
651 *Quarterly Journal of the Royal Meteorological Society*, **130**, 3119-3137, 10.1256/qj.03.103.
- 652 Bechtold, P., and Coauthors, 2008: Advances in simulating atmospheric variability with the ECMWF  
653 model: From synoptic to decadal time-scales. *Quarterly Journal of the Royal Meteorological Society*,  
654 **134**, 1337-1351, <https://doi.org/10.1002/qj.289>.
- 655 Bechtold, P., N. Semane, P. Lopez, J.-P. Chaboureau, A. Beljaars, and N. Bormann, 2014: Representing  
656 Equilibrium and Nonequilibrium Convection in Large-Scale Models. *Journal of the Atmospheric*  
657 *Sciences*, **71**, 734-753, 10.1175/jas-d-13-0163.1.
- 658 Betts, A. K., and C. Jakob, 2002: Study of diurnal cycle of convective precipitation over Amazonia using  
659 a single column model. *Journal of Geophysical Research: Atmospheres*, **107**, ACL 25-1-ACL 25-13,  
660 10.1029/2002jd002264.
- 661 Bogenschutz, P. A., S. Tang, P. M. Caldwell, S. Xie, W. Lin, and Y. S. Chen, 2020: The E3SM version 1  
662 single-column model. *Geosci. Model Dev.*, **13**, 4443-4458, 10.5194/gmd-13-4443-2020.
- 663 Bretherton, C. S., S. K. Krueger, M. C. Wyant, P. Bechtold, E. Van Meijgaard, B. Stevens, and J.  
664 Teixeira, 1999: A GCSS Boundary-Layer Cloud Model Intercomparison Study Of The First Astex  
665 Lagrangian Experiment. *Boundary-Layer Meteorology*, **93**, 341-380, 10.1023/A:1002005429969.
- 666 Bretherton, C. S., M. E. Peters, and L. E. Back, 2004: Relationships between Water Vapor Path and  
667 Precipitation over the Tropical Oceans. *Journal of Climate*, **17**, 1517-1528, 10.1175/1520-  
668 0442(2004)017<1517:Rbwvpa>2.0.Co;2.
- 669 Bretherton, C. S., and S. Park, 2009: A New Moist Turbulence Parameterization in the Community  
670 Atmosphere Model. *Journal of Climate*, **22**, 3422-3448, 10.1175/2008JCLI2556.1.
- 671 Covey, C., and Coauthors, 2016: Metrics for the Diurnal Cycle of Precipitation: Toward Routine  
672 Benchmarks for Climate Models. *Journal of Climate*, **29**, 4461-4471, 10.1175/jcli-d-15-0664.1.
- 673 Cui, Z., G. J. Zhang, Y. Wang, and S. Xie, 2021: Understanding the Roles of Convective Trigger  
674 Functions in the Diurnal Cycle of Precipitation in the NCAR CAM5. *Journal of Climate*, **34**, 6473-6489,  
675 10.1175/jcli-d-20-0699.1.
- 676 Dai, A., K. E. Trenberth, and T. R. Karl, 1999: Effects of Clouds, Soil Moisture, Precipitation, and Water  
677 Vapor on Diurnal Temperature Range. *Journal of Climate*, **12**, 2451-2473, 10.1175/1520-  
678 0442(1999)012<2451:Eocsmv>2.0.Co;2.

- 1  
2  
3 679 Dai, A., 2006: Precipitation Characteristics in Eighteen Coupled Climate Models. *Journal of Climate*, **19**,  
4 680 4605-4630, 10.1175/jcli3884.1.
- 5  
6 681 Davies, L., and Coauthors, 2013: A single-column model ensemble approach applied to the TWP-ICE  
7 682 experiment. *Journal of Geophysical Research: Atmospheres*, **118**, 6544-6563, 10.1002/jgrd.50450.
- 8  
9 683 de Rooy, W. C., and Coauthors, 2013: Entrainment and detrainment in cumulus convection: an overview.  
10 684 *Quarterly Journal of the Royal Meteorological Society*, **139**, 1-19, 10.1002/qj.1959.
- 11 685 Del Genio, A. D., Y. Chen, D. Kim, and M.-S. Yao, 2012: The MJO Transition from Shallow to Deep  
12 686 Convection in CloudSat/CALIPSO Data and GISS GCM Simulations. *Journal of Climate*, **25**, 3755-3770,  
13 687 10.1175/jcli-d-11-00384.1.
- 14  
15 688 Eyring, V., S. Bony, G. A. Meehl, C. A. Senior, B. Stevens, R. J. Stouffer, and K. E. Taylor, 2016:  
16 689 Overview of the Coupled Model Intercomparison Project Phase 6 (CMIP6) experimental design and  
17 690 organization. *Geosci. Model Dev.*, **9**, 1937-1958, 10.5194/gmd-9-1937-2016.
- 18  
19 691 Fiedler, S., and Coauthors, 2020: Simulated Tropical Precipitation Assessed across Three Major Phases of  
20 692 the Coupled Model Intercomparison Project (CMIP). *Monthly Weather Review*, **148**, 3653-3680,  
21 693 10.1175/mwr-d-19-0404.1.
- 22  
23 694 Frenkel, Y., B. Khouider, and A. J. Majda, 2011a: Simple Multicloud Models for the Diurnal Cycle of  
24 695 Tropical Precipitation. Part I: Formulation and the Case of the Tropical Oceans. *Journal of the  
25 696 Atmospheric Sciences*, **68**, 2169-2190, 10.1175/2011jas3568.1.
- 26  
27 697 ———, 2011b: Simple Multicloud Models for the Diurnal Cycle of Tropical Precipitation. Part II: The  
28 698 Continental Regime. *Journal of the Atmospheric Sciences*, **68**, 2192-2207, 10.1175/2011jas3600.1.
- 29  
30 699 Geerts, B., and Coauthors, 2017: The 2015 Plains Elevated Convection at Night Field Project. *Bulletin of  
700 the American Meteorological Society*, **98**, 767-786, 10.1175/bams-d-15-00257.1.
- 31  
32 701 Gettelman, A., H. Morrison, S. Santos, P. Bogenschutz, and P. M. Caldwell, 2015: Advanced Two-  
33 702 Moment Bulk Microphysics for Global Models. Part II: Global Model Solutions and Aerosol-Cloud  
34 703 Interactions. *Journal of Climate*, **28**, 1288-1307, 10.1175/jcli-d-14-00103.1.
- 35  
36 704 Gettelman, A., J. E. Truesdale, J. T. Bacmeister, P. M. Caldwell, R. B. Neale, P. A. Bogenschutz, and I.  
37 705 R. Simpson, 2019: The Single Column Atmosphere Model Version 6 (SCAM6): Not a Scam but a Tool  
38 706 for Model Evaluation and Development. *Journal of Advances in Modeling Earth Systems*, **11**, 1381-1401,  
39 707 10.1029/2018ms001578.
- 40  
41 708 Ghan, S., and Coauthors, 2000: A comparison of single column model simulations of summertime  
42 709 midlatitude continental convection. *Journal of Geophysical Research: Atmospheres*, **105**, 2091-2124,  
43 710 10.1029/1999JD900971.
- 44  
45 711 Golaz, J.-C., V. E. Larson, and W. R. Cotton, 2002: A PDF-Based Model for Boundary Layer Clouds.  
46 712 Part I: Method and Model Description. *Journal of the Atmospheric Sciences*, **59**, 3540-3551,  
47 713 10.1175/1520-0469(2002)059<3540:apbmf>2.0.co;2.
- 48  
49 714 Griffin, B. M., and V. E. Larson, 2016: Parameterizing microphysical effects on variances and  
50 715 covariances of moisture and heat content using a multivariate probability density function: a study with  
51 716 CLUBB (tag MVCS). *Geosci. Model Dev.*, **9**, 4273-4295, 10.5194/gmd-9-4273-2016.
- 52  
53 717 Guichard, F., and Coauthors, 2004: Modelling the diurnal cycle of deep precipitating convection over  
54 718 land with cloud-resolving models and single-column models. *Quarterly Journal of the Royal  
55 719 Meteorological Society*, **130**, 3139-3172, 10.1256/qj.03.145.
- 56  
57 720 Guo, Z., B. M. Griffin, S. Domke, and V. E. Larson, 2021: A parameterization of turbulent dissipation  
58 721 and pressure damping time scales in stably stratified inversions, and its effects on low clouds in global  
59  
60

- 1  
2  
3 722 simulations. *Journal of Advances in Modeling Earth Systems*, **n/a**, e2020MS002278,  
4 723 <https://doi.org/10.1029/2020MS002278>.  
5  
6 724 Han, J.-Y., S.-Y. Hong, and Y. C. Kwon, 2020: The Performance of a Revised Simplified Arakawa–  
7 725 Schubert (SAS) Convection Scheme in the Medium-Range Forecasts of the Korean Integrated Model  
8 726 (KIM). *Weather and Forecasting*, **35**, 1113-1128, 10.1175/waf-d-19-0219.1.  
9  
10 727 Han, J., and H.-L. Pan, 2011: Revision of Convection and Vertical Diffusion Schemes in the NCEP  
11 728 Global Forecast System. *Weather and Forecasting*, **26**, 520-533, 10.1175/waf-d-10-05038.1.  
12 729 Hohenegger, C., and B. Stevens, 2013: Preconditioning Deep Convection with Cumulus Congestus.  
13 730 *Journal of the Atmospheric Sciences*, **70**, 448-464, 10.1175/jas-d-12-089.1.  
14  
15 731 Holloway, C. E., and J. D. Neelin, 2009: Moisture Vertical Structure, Column Water Vapor, and Tropical  
16 732 Deep Convection. *Journal of the Atmospheric Sciences*, **66**, 1665-1683, 10.1175/2008jas2806.1.  
17 733 Holtslag, A. A. M., and B. A. Boville, 1993: Local Versus Nonlocal Boundary-Layer Diffusion in a  
18 734 Global Climate Model. *Journal of Climate*, **6**, 1825-1842, 10.1175/1520-  
19 735 0442(1993)006<1825:Lvnbl>2.0.Co;2.  
20  
21 736 Hong, S.-Y., J. Dudhia, and S.-H. Chen, 2004: A Revised Approach to Ice Microphysical Processes for  
22 737 the Bulk Parameterization of Clouds and Precipitation. *Monthly Weather Review*, **132**, 103-120,  
23 738 10.1175/1520-0493(2004)132<0103:Aratim>2.0.Co;2.  
24  
25 739 Hong, S.-Y., and Coauthors, 2013: The Global/Regional Integrated Model system (GRIMs). *Asia-Pacific*  
26 740 *Journal of Atmospheric Sciences*, **49**, 219-243, 10.1007/s13143-013-0023-0.  
27 741 Hong, S.-Y., and Coauthors, 2018: The Korean Integrated Model (KIM) System for Global Weather  
28 742 Forecasting. *Asia-Pacific Journal of Atmospheric Sciences*, **54**, 267-292, 10.1007/s13143-018-0028-9.  
29  
30 743 Kain, J. S., and J. M. Fritsch, 1990: A One-Dimensional Entraining/Detraining Plume Model and Its  
31 744 Application in Convective Parameterization. *Journal of Atmospheric Sciences*, **47**, 2784-2802,  
32 745 10.1175/1520-0469(1990)047<2784:Aodepm>2.0.Co;2.  
33  
34 746 ———, 1992: The role of the convective “trigger function” in numerical forecasts of mesoscale convective  
35 747 systems. *Meteorol. Atmos. Phys.*, **49**, 93-106, 10.1007/BF01025402.  
36 748 Khairoutdinov, M., and D. Randall, 2006: High-Resolution Simulation of Shallow-to-Deep Convection  
37 749 Transition over Land. *Journal of the Atmospheric Sciences*, **63**, 3421-3436, 10.1175/jas3810.1.  
38  
39 750 Khouider, B., and E. Leclerc, 2019: Toward a Stochastic Relaxation for the Quasi-Equilibrium Theory of  
40 751 Cumulus Parameterization: Multicloud Instability, Multiple Equilibria, and Chaotic Dynamics. *Journal of*  
41 752 *Advances in Modeling Earth Systems*, **11**, 2474-2502.  
42  
43 753 Khouider, B., B. Goswami, R. Phani, and A. Majda, 2021: A shallow-deep unified stochastic mass-flux  
44 754 cumulus parameterization in the single column Community Climate Model. *Journal of Advances in*  
45 755 *Modeling Earth Systems*, Under Review.  
46 756 Kim, S.-Y., and S.-Y. Hong, 2018: The Use of Partial Cloudiness in a Bulk Cloud Microphysics Scheme:  
47 757 Concept and 2D Results. *Journal of the Atmospheric Sciences*, **75**, 2711-2719, 10.1175/jas-d-17-0234.1.  
48  
49 758 Klein, S. A., and Coauthors, 2009: Intercomparison of model simulations of mixed-phase clouds observed  
50 759 during the ARM Mixed-Phase Arctic Cloud Experiment. I: single-layer cloud. *Quarterly Journal of the*  
51 760 *Royal Meteorological Society*, **135**, 979-1002, 10.1002/qj.416.  
52  
53 761 Köhler, M., 2020: Cloud cover. *Chapter 3.8.5 in ICON Tutorial: Working with the ICON Model*, F. Prill,  
54 762 D. Reinert, D. Rieger, and G. Zängl, November 2020, 10.5676/dwd\_pub/nwv/icon\_tutorial2020.  
55 763  
56  
57  
58  
59  
60

- 1  
2  
3 764 Koo, M.-S., and S.-Y. Hong, 2010: Diurnal variations of simulated precipitation over East Asia in two  
4 765 regional climate models. *Journal of Geophysical Research: Atmospheres*, **115**,  
5 766 <https://doi.org/10.1029/2009JD012574>.
- 6  
7 767 Koo, M.-S., S. Baek, K.-H. Seol, and K. Cho, 2017: Advances in land modeling of KIAPS based on the  
8 768 Noah Land Surface Model. *Asia-Pacific Journal of Atmospheric Sciences*, **53**, 361-373, 10.1007/s13143-  
9 769 017-0043-2.
- 10  
11 770 Kuo, Y.-H., K. A. Schiro, and J. D. Neelin, 2018: Convective Transition Statistics over Tropical Oceans  
12 771 for Climate Model Diagnostics: Observational Baseline. *Journal of the Atmospheric Sciences*, **75**, 1553-  
13 772 1570, 10.1175/jas-d-17-0287.1.
- 14  
15 773 Kuo, Y.-H., and Coauthors, 2020: Convective Transition Statistics over Tropical Oceans for Climate  
16 774 Model Diagnostics: GCM Evaluation. *Journal of the Atmospheric Sciences*, **77**, 379-403, 10.1175/jas-d-  
17 775 19-0132.1.
- 18  
19 776 Larson, V. E., and J.-C. Golaz, 2005: Using Probability Density Functions to Derive Consistent Closure  
20 777 Relationships among Higher-Order Moments. *Monthly Weather Review*, **133**, 1023-1042,  
21 778 10.1175/mwr2902.1.
- 22  
23 779 Larson, V. E., and D. P. Schanen, 2013: The Subgrid Importance Latin Hypercube Sampler (SILHS): a  
24 780 multivariate subcolumn generator. *Geosci. Model Dev.*, **6**, 1813-1829, 10.5194/gmd-6-1813-2013.
- 25  
26 781 Larson, V. E., 2017: CLUBB-SILHS: A parameterization of subgrid variability in the atmosphere,  
27 782 ArXiv:1711.03675 [Physics].
- 28  
29 783 Lawrence, D. M., and Coauthors, 2019: The Community Land Model Version 5: Description of New  
30 784 Features, Benchmarking, and Impact of Forcing Uncertainty. *Journal of Advances in Modeling Earth*  
31 785 *Systems*, **11**, 4245-4287, <https://doi.org/10.1029/2018MS001583>.
- 32  
33 786 Lee, E.-H., E. Lee, R. Park, Y. C. Kwon, and S.-Y. Hong, 2018: Impact of Turbulent Mixing in the  
34 787 Stratocumulus-Topped Boundary Layer on Numerical Weather Prediction. *Asia-Pacific Journal of*  
35 788 *Atmospheric Sciences*, **54**, 371-384, 10.1007/s13143-018-0024-0.
- 36  
37 789 Lee, M.-I., S. D. Schubert, M. J. Suarez, J.-K. E. Schemm, H.-L. Pan, J. Han, and S.-H. Yoo, 2008: Role  
38 790 of convection triggers in the simulation of the diurnal cycle of precipitation over the United States Great  
39 791 Plains in a general circulation model. *Journal of Geophysical Research: Atmospheres*, **113**,  
40 792 doi:10.1029/2007JD008984.
- 41  
42 793 Lee, W. L., and Coauthors, 2020: Taiwan Earth System Model Version 1: Description and Evaluation of  
43 794 Mean State. *Geosci. Model Dev. Discuss.*, **2020**, 1-43, 10.5194/gmd-2019-377.
- 44  
45 795 Lenderink, G., and Coauthors, 2004: The diurnal cycle of shallow cumulus clouds over land: A single-  
46 796 column model intercomparison study. *Quarterly Journal of the Royal Meteorological Society*, **130**, 3339-  
47 797 3364, 10.1256/qj.03.122.
- 48  
49 798 Lin, W., and S. Xie, 2021: Frameworks for Testing and Evaluating Fast Physics Parameterizations in  
50 799 Climate and Weather Forecasting Models. *Fast Physics in Large Scale Atmospheric Models:*  
51 800 *Parameterization, Evaluation, and Observations*, Y. Liu, P. Kollias, and L. J. Donner, Eds., in publish.
- 52  
53 801 Ma, H.-Y., K. Zhang, S. Tang, S. Xie, and R. Fu, 2021a: Evaluation of the Causes of Wet-Season Dry  
54 802 Biases Over Amazonia in CAM5. *Journal of Geophysical Research: Atmospheres*, **126**, e2020JD033859,  
55 803 <https://doi.org/10.1029/2020JD033859>.
- 56  
57 804 Ma, H. Y., and Coauthors, 2021b: A multi-year short-range hindcast experiment with CESM1 for  
58 805 evaluating climate model moist processes from diurnal to interannual timescales. *Geosci. Model Dev.*, **14**,  
59 806 73-90, 10.5194/gmd-14-73-2021.

- 1  
2  
3 807 Malardel, S., and P. Bechtold, 2019: The coupling of deep convection with the resolved flow via the  
4 808 divergence of mass flux in the IFS. *Quarterly Journal of the Royal Meteorological Society*, **145**, 1832-  
5 809 1845, <https://doi.org/10.1002/qj.3528>.  
6  
7 810 Mapes, B., and R. Neale, 2011: Parameterizing Convective Organization to Escape the Entrainment  
8 811 Dilemma. *Journal of Advances in Modeling Earth Systems*, **3**, <https://doi.org/10.1029/2011MS000042>.  
9  
10 812 Martin, S. T., and Coauthors, 2016: Introduction: Observations and Modeling of the Green Ocean  
11 813 Amazon (GoAmazon2014/5). *Atmos. Chem. Phys.*, **16**, 4785-4797, 10.5194/acp-16-4785-2016.  
12 814 McTaggart-Cowan, R., and Coauthors, 2019a: Modernization of Atmospheric Physics Parameterization  
13 815 in Canadian NWP. *Journal of Advances in Modeling Earth Systems*, **n/a**, 10.1029/2019ms001781.  
14  
15 816 McTaggart-Cowan, R., P. A. Vaillancourt, A. Zadra, L. Separovic, S. Corvec, and D. Kirshbaum, 2019b:  
16 817 A Lagrangian Perspective on Parameterizing Deep Convection. *Monthly Weather Review*, **147**, 4127-  
17 818 4149, 10.1175/mwr-d-19-0164.1.  
18 819 McTaggart-Cowan, R., P. A. Vaillancourt, L. Separovic, S. Corvec, and A. Zadra, 2020: A Convection  
19 820 Parameterization for Low-CAPE Environments. *Monthly Weather Review*, **148**, 4917-4941,  
20 821 10.1175/mwr-d-20-0020.1.  
21  
22 822 Morrison, H., and A. Gettelman, 2008: A New Two-Moment Bulk Stratiform Cloud Microphysics  
23 823 Scheme in the Community Atmosphere Model, Version 3 (CAM3). Part I: Description and Numerical  
24 824 Tests. *Journal of Climate*, **21**, 3642-3659, 10.1175/2008JCLI2105.1.  
25  
26 825 Morrison, H., and Coauthors, 2009: Intercomparison of model simulations of mixed-phase clouds  
27 826 observed during the ARM Mixed-Phase Arctic Cloud Experiment. II: Multilayer cloud. *Quarterly*  
28 827 *Journal of the Royal Meteorological Society*, **135**, 1003-1019, 10.1002/qj.415.  
29 828 Neale, R. B., and Coauthors, 2012: Description of the NCAR Community Atmosphere Model (CAM 5.0).  
30 829 NCAR Technical Note NCARTN-4861STR, 274 pp.  
31  
32 830 Neelin, J. D., O. Peters, and K. Hales, 2009: The Transition to Strong Convection. *Journal of the*  
33 831 *Atmospheric Sciences*, **66**, 2367-2384, 10.1175/2009jas2962.1.  
34  
35 832 Neggers, R. A. J., A. P. Siebesma, and T. Heus, 2012: Continuous Single-Column Model Evaluation at a  
36 833 Permanent Meteorological Supersite. *Bulletin of the American Meteorological Society*, **93**, 1389-1400,  
37 834 10.1175/bams-d-11-00162.1.  
38 835 Neggers, R. A. J., and A. P. Siebesma, 2013: Constraining a System of Interacting Parameterizations  
39 836 through Multiple-Parameter Evaluation: Tracing a Compensating Error between Cloud Vertical Structure  
40 837 and Cloud Overlap. *Journal of Climate*, **26**, 6698-6715, 10.1175/jcli-d-12-00779.1.  
41  
42 838 Neggers, R. A. J., 2015a: Exploring bin-macrophysics models for moist convective transport and clouds.  
43 839 *Journal of Advances in Modeling Earth Systems*, **7**, 2079-2104, 10.1002/2015ms000502.  
44 840 ———, 2015b: Attributing the behavior of low-level clouds in large-scale models to subgrid-scale  
45 841 parameterizations. *Journal of Advances in Modeling Earth Systems*, **7**, 2029-2043,  
46 842 <https://doi.org/10.1002/2015MS000503>.  
47  
48 843 Neggers, R. A. J., and Coauthors, 2017: Single-Column Model Simulations of Subtropical Marine  
49 844 Boundary-Layer Cloud Transitions Under Weakening Inversions. *Journal of Advances in Modeling Earth*  
50 845 *Systems*, **9**, 2385-2412, <https://doi.org/10.1002/2017MS001064>.  
51  
52 846 Oliveira, M. I., and Coauthors, 2020: Planetary boundary layer evolution over the Amazon rainforest in  
53 847 episodes of deep moist convection at the Amazon Tall Tower Observatory. *Atmos. Chem. Phys.*, **20**, 15-  
54 848 27, 10.5194/acp-20-15-2020.  
55  
56  
57  
58  
59  
60

- 1  
2  
3 849 Park, R.-S., J.-H. Chae, and S.-Y. Hong, 2016: A Revised Prognostic Cloud Fraction Scheme in a Global  
4 850 Forecasting System. *Monthly Weather Review*, **144**, 1219-1229, 10.1175/mwr-d-15-0273.1.
- 5  
6 851 Park, S., and C. S. Bretherton, 2009: The University of Washington Shallow Convection and Moist  
7 852 Turbulence Schemes and Their Impact on Climate Simulations with the Community Atmosphere Model.  
8 853 *Journal of Climate*, **22**, 3449-3469, 10.1175/2008JCLI2557.1.
- 9  
10 854 Park, S., 2014a: A Unified Convection Scheme (UNICON). Part I: Formulation. *Journal of the*  
11 855 *Atmospheric Sciences*, **71**, 3902-3930, 10.1175/jas-d-13-0233.1.
- 12 856 ———, 2014b: A Unified Convection Scheme (UNICON). Part II: Simulation. *Journal of the Atmospheric*  
13 857 *Sciences*, **71**, 3931-3973, 10.1175/jas-d-13-0234.1.
- 14  
15 858 Park, S., C. S. Bretherton, and P. J. Rasch, 2014: Integrating Cloud Processes in the Community  
16 859 Atmosphere Model, Version 5. *Journal of Climate*, **27**, 6821-6856, 10.1175/JCLI-D-14-00087.1.
- 17 860 Park, S., E.-H. Baek, B.-M. Kim, and S.-J. Kim, 2017: Impact of detrained cumulus on climate simulated  
18 861 by the Community Atmosphere Model Version 5 with a unified convection scheme. *Journal of Advances*  
19 862 *in Modeling Earth Systems*, **9**, 1399-1411, <https://doi.org/10.1002/2016MS000877>.
- 20  
21 863 Park, S., J. Shin, S. Kim, E. Oh, and Y. Kim, 2019: Global Climate Simulated by the Seoul National  
22 864 University Atmosphere Model Version 0 with a Unified Convection Scheme (SAM0-UNICON). *Journal*  
23 865 *of Climate*, **32**, 2917-2949, 10.1175/jcli-d-18-0796.1.
- 24  
25 866 Petch, J., and Coauthors, 2014: Evaluation of intercomparisons of four different types of model  
26 867 simulating TWP-ICE. *Quarterly Journal of the Royal Meteorological Society*, **140**, 826-837,  
27 868 10.1002/qj.2192.
- 28  
29 869 Pithan, F., and Coauthors, 2016: Select strengths and biases of models in representing the Arctic winter  
30 870 boundary layer over sea ice: the Larcform 1 single column model intercomparison. *Journal of Advances*  
31 871 *in Modeling Earth Systems*, **8**, 1345-1357, <https://doi.org/10.1002/2016MS000630>.
- 32 872 Randall, D. A., K.-M. Xu, R. J. C. Somerville, and S. Iacobellis, 1996: Single-Column Models and Cloud  
33 873 Ensemble Models as Links between Observations and Climate Models. *Journal of Climate*, **9**, 1683-1697,  
34 874 10.1175/1520-0442(1996)009<1683:SCMACE>2.0.CO;2.
- 35  
36 875 Rasch, P. J., and Coauthors, 2019: An Overview of the Atmospheric Component of the Energy Exascale  
37 876 Earth System Model. *Journal of Advances in Modeling Earth Systems*, **11**, 2377-2411,  
38 877 10.1029/2019ms001629.
- 39  
40 878 Raschendorfer, M., 2000: The New Turbulence Parameterization in the Lokal-Modell of DWD. *Research*  
41 879 *Activities in Atmospheric and Oceanic Modelling*, WMO/TD-No.987, pg 4.30-4.31.
- 42 880 Rio, C., F. Hourdin, J. Y. Grandpeix, and J. P. Lafore, 2009: Shifting the diurnal cycle of parameterized  
43 881 deep convection over land. *Geophysical Research Letters*, **36**, 10.1029/2008GL036779.
- 44  
45 882 Ruppert, J. H., and R. H. Johnson, 2015: Diurnally Modulated Cumulus Moistening in the Preonset Stage  
46 883 of the Madden-Julian Oscillation during DYNAMO. *Journal of the Atmospheric Sciences*, **72**, 1622-  
47 884 1647, 10.1175/JAS-D-14-0218.1.
- 48  
49 885 Rutledge, S. A., and P. V. Hobbs, 1984: The Mesoscale and Microscale Structure and Organization of  
50 886 Clouds and Precipitation in Midlatitude Cyclones. XII: A Diagnostic Modeling Study of Precipitation  
51 887 Development in Narrow Cold-Frontal Rainbands. *Journal of Atmospheric Sciences*, **41**, 2949-2972,  
52 888 10.1175/1520-0469(1984)041<2949:Tmamsa>2.0.Co;2.
- 53 889 Schumacher, C., R. A. Houze, and I. Kraucunas, 2004: The Tropical Dynamical Response to Latent  
54 890 Heating Estimates Derived from the TRMM Precipitation Radar. *Journal of the Atmospheric Sciences*,  
55 891 **61**, 1341-1358, 10.1175/1520-0469(2004)061<1341:TTDRTL>2.0.CO;2.
- 56  
57  
58  
59  
60

- 1  
2  
3 892 Seifert, A., 2008: A Revised Cloud Microphysical Parameterization for COSMO-LME. *COSMO Newsl*,  
4 893 7, 25-28, <http://www.cosmo->  
5 894 [model.org/content/model/documentation/newsLetters/newsLetter07/cnl7\\_seifert.pdf](http://www.cosmo-model.org/content/model/documentation/newsLetters/newsLetter07/cnl7_seifert.pdf).  
6  
7 895 Shin, H. H., and S.-Y. Hong, 2015: Representation of the Subgrid-Scale Turbulent Transport in  
8 896 Convective Boundary Layers at Gray-Zone Resolutions. *Monthly Weather Review*, **143**, 250-271,  
9 897 10.1175/mwr-d-14-00116.1.
- 10 898 Shiu, C. J., and Coauthors, 2021: GTS v1.0: a macrophysics scheme for climate models based on a  
11 899 probability density function. *Geosci. Model Dev.*, **14**, 177-204, 10.5194/gmd-14-177-2021.
- 12 900 Stephens, G. L., and Coauthors, 2010: Dreary state of precipitation in global models. *Journal of*  
13 901 *Geophysical Research: Atmospheres*, **115**, <https://doi.org/10.1029/2010JD014532>.  
14  
15 902 Stratton, R. A., and A. J. Stirling, 2012: Improving the diurnal cycle of convection in GCMs. *Quarterly*  
16 903 *Journal of the Royal Meteorological Society*, **138**, 1121-1134, 10.1002/qj.991.
- 17 904 Sun, Y., S. Solomon, A. Dai, and R. W. Portmann, 2007: How Often Will It Rain? *Journal of Climate*,  
18 905 **20**, 4801-4818, 10.1175/jcli4263.1.
- 19 906 Sundqvist, H., E. Berge, and J. E. Kristjánsson, 1989: Condensation and Cloud Parameterization Studies  
20 907 with a Mesoscale Numerical Weather Prediction Model. *Monthly Weather Review*, **117**, 1641-1657,  
21 908 10.1175/1520-0493(1989)117<1641:Cacpsw>2.0.Co;2.
- 22 909 Tang, S., and Coauthors, 2016: Large-scale vertical velocity, diabatic heating and drying profiles  
23 910 associated with seasonal and diurnal variations of convective systems observed in the GoAmazon2014/5  
24 911 experiment. *Atmos. Chem. Phys.*, **16**, 14249-14264, 10.5194/acp-16-14249-2016.
- 25 912 Tang, S., and Coauthors, 2019: Differences in Eddy-Correlation and Energy-Balance Surface Turbulent  
26 913 Heat Flux Measurements and Their Impacts on the Large-Scale Forcing Fields at the ARM SGP Site.  
27 914 *Journal of Geophysical Research: Atmospheres*, **124**, 3301-3318, 10.1029/2018jd029689.
- 28 915 Tang, S., P. Gleckler, S. Xie, J. Lee, M.-S. Ahn, C. Covey, and C. Zhang, 2021: Evaluating the Diurnal  
29 916 and Semidiurnal Cycle of Precipitation in CMIP6 Models Using Satellite- and Ground-Based  
30 917 Observations. *Journal of Climate*, **34**, 3189-3210, 10.1175/jcli-d-20-0639.1.
- 31 918 Taylor, K. E., R. J. Stouffer, and G. A. Meehl, 2012: An Overview of CMIP5 and the Experiment Design.  
32 919 *Bulletin of the American Meteorological Society*, **93**, 485-498, 10.1175/bams-d-11-00094.1.
- 33 920 Thayer-Calder, K., and Coauthors, 2015: A unified parameterization of clouds and turbulence using  
34 921 CLUBB and subcolumns in the Community Atmosphere Model. *Geosci. Model Dev.*, **8**, 3801-3821,  
35 922 10.5194/gmd-8-3801-2015.
- 36 923 Tian, Y., Y. Zhang, S. A. Klein, and C. Schumacher, 2021: Interpreting the Diurnal Cycle of Clouds and  
37 924 Precipitation in the ARM GoAmazon Observations: Shallow to Deep Convection Transition. *Journal of*  
38 925 *Geophysical Research: Atmospheres*, **126**, e2020JD033766, <https://doi.org/10.1029/2020JD033766>.  
39  
40 926 Trenberth, K. E., A. Dai, R. M. Rasmussen, and D. B. Parsons, 2003: The Changing Character of  
41 927 Precipitation. *Bulletin of the American Meteorological Society*, **84**, 1205-1218, 10.1175/bams-84-9-1205.
- 42 928 Varble, A. C., and Coauthors, 2021: Utilizing a Storm-Generating Hotspot to Study Convective Cloud  
43 929 Transitions: The CACTI Experiment. *Bulletin of the American Meteorological Society*, **102**, E1597-  
44 930 E1620, 10.1175/bams-d-20-0030.1.
- 45 931 Wang, Y.-C., and H.-H. Hsu, 2019: Improving diurnal rainfall phase over the Southern Great Plains in  
46 932 warm seasons by using a convective triggering design. *International Journal of Climatology*, **39**, 5181-  
47 933 5190, 10.1002/joc.6117.
- 48  
49  
50  
51  
52  
53  
54  
55  
56  
57  
58  
59  
60

- 1  
2  
3 934 Wang, Y.-C., S. Xie, S. Tang, and W. Lin, 2020: Evaluation of an Improved Convective Triggering  
4 935 Function: Observational Evidence and SCM Tests. *Journal of Geophysical Research: Atmospheres*, **125**,  
5 936 e2019JD031651, 10.1029/2019jd031651.
- 6  
7 937 Wang, Y., L. Zhou, and K. Hamilton, 2007: Effect of Convective Entrainment/Detrainment on the  
8 938 Simulation of the Tropical Precipitation Diurnal Cycle. *Monthly Weather Review*, **135**, 567-585,  
9 939 10.1175/mwr3308.1.
- 10  
11 940 Wang, Y. C., H. L. Pan, and H. H. Hsu, 2015: Impacts of the triggering function of cumulus  
12 941 parameterization on warm-season diurnal rainfall cycles at the Atmospheric Radiation Measurement  
13 942 Southern Great Plains site. *Journal of Geophysical Research: Atmospheres*, **120**, 10,681-10,702,  
14 943 doi:10.1002/2015JD023337.
- 15  
16 944 Wei, Y., Z. Pu, and C. Zhang, 2020: Diurnal Cycle of Precipitation Over the Maritime Continent Under  
17 945 Modulation of MJO: Perspectives From Cloud-Permitting Scale Simulations. *Journal of Geophysical*  
18 946 *Research: Atmospheres*, **125**, e2020JD032529, <https://doi.org/10.1029/2020JD032529>.
- 19  
20 947 Wyant, M. C., and Coauthors, 2007: A single-column model intercomparison of a heavily drizzling  
21 948 stratocumulus-topped boundary layer. *Journal of Geophysical Research: Atmospheres*, **112**,  
22 949 10.1029/2007jd008536.
- 23  
24 950 Xie, S., and M. Zhang, 2000: Impact of the convection triggering function on single-column model  
25 951 simulations. *Journal of Geophysical Research: Atmospheres*, **105**, 14983-14996,  
26 952 doi:10.1029/2000JD900170.
- 27  
28 953 Xie, S., and Coauthors, 2002: Intercomparison and evaluation of cumulus parametrizations under  
29 954 summertime midlatitude continental conditions. *Quarterly Journal of the Royal Meteorological Society*,  
30 955 **128**, 1095-1135, 10.1256/003590002320373229.
- 31  
32 956 Xie, S., R. T. Cederwall, and M. Zhang, 2004: Developing long-term single-column model/cloud system-  
33 957 resolving model forcing data using numerical weather prediction products constrained by surface and top  
34 958 of the atmosphere observations. *Journal of Geophysical Research*, **109**, 10.1029/2003jd004045.
- 35  
36 959 Xie, S., and Coauthors, 2005: Simulations of midlatitude frontal clouds by single-column and cloud-  
37 960 resolving models during the Atmospheric Radiation Measurement March 2000 cloud intensive  
38 961 operational period. *Journal of Geophysical Research: Atmospheres*, **110**, D15S03,  
39 962 10.1029/2004JD005119.
- 40  
41 963 Xie, S., and Coauthors, 2018: Understanding Cloud and Convective Characteristics in Version 1 of the  
42 964 E3SM Atmosphere Model. *Journal of Advances in Modeling Earth Systems*, **10**, 2618-2644,  
43 965 doi:10.1029/2018MS001350.
- 44  
45 966 Xie, S., and Coauthors, 2019: Improved Diurnal Cycle of Precipitation in E3SM With a Revised  
46 967 Convective Triggering Function. *Journal of Advances in Modeling Earth Systems*, **11**, 2290-2310,  
47 968 10.1029/2019ms001702.
- 48  
49 969 Xu, K.-M., and Coauthors, 2005: Modeling springtime shallow frontal clouds with cloud-resolving and  
50 970 single-column models. *Journal of Geophysical Research: Atmospheres*, **110**, 10.1029/2004JD005153.
- 51  
52 971 Yanai, M., S. Esbensen, and J.-H. Chu, 1973: Determination of Bulk Properties of Tropical Cloud  
53 972 Clusters from Large-Scale Heat and Moisture Budgets. *Journal of the Atmospheric Sciences*, **30**, 611-627,  
54 973 10.1175/1520-0469(1973)030<0611:DOBPOT>2.0.CO;2.
- 55  
56 974 Zängl, G., D. Reinert, P. Ripodas, and M. Baldauf, 2015: The ICON (ICOsahedral Non-hydrostatic)  
57 975 modelling framework of DWD and MPI-M: Description of the non-hydrostatic dynamical core. *Quarterly*  
58 976 *Journal of the Royal Meteorological Society*, **141**, 563-579, <https://doi.org/10.1002/qj.2378>.
- 59  
60

- 1  
2  
3 977 Zermeño-Díaz, D. M., C. Zhang, P. Kollias, and H. Kalesse, 2015: The Role of Shallow Cloud  
4 978 Moistening in MJO and Non-MJO Convective Events over the ARM Manus Site. *Journal of the*  
5 979 *Atmospheric Sciences*, **72**, 4797-4820, 10.1175/JAS-D-14-0322.1.  
6  
7 980 Zhang, G. J., and N. A. McFarlane, 1995: Sensitivity of climate simulations to the parameterization of  
8 981 cumulus convection in the Canadian climate centre general circulation model. *Atmosphere-Ocean*, **33**,  
9 982 407-446, 10.1080/07055900.1995.9649539.  
10  
11 983 Zhang, G. J., 2003: Roles of tropospheric and boundary layer forcing in the diurnal cycle of convection in  
12 984 the U.S. southern great plains. *Geophysical Research Letters*, **30**, doi:10.1029/2003GL018554.  
13  
14 985 Zhang, M., and J. Lin, 1997: Constrained Variational Analysis of Sounding Data Based on Column-  
15 986 Integrated Budgets of Mass, Heat, Moisture, and Momentum: Approach and Application to ARM  
16 987 Measurements. *Journal of the Atmospheric Sciences*, **54**, 1503-1524, 10.1175/1520-  
17 988 0469(1997)054<1503:CVAOSD>2.0.CO;2.  
18  
19 989 Zhang, M., J. Lin, R. T. Cederwall, J. J. Yio, and S. C. Xie, 2001: Objective Analysis of ARM IOP Data:  
20 990 Method and Sensitivity. *Monthly Weather Review*, **129**, 295-311, 10.1175/1520-  
21 991 0493(2001)129<0295:OAOAID>2.0.CO;2.  
22  
23 992 Zhang, M., R. C. J. Somerville, and S. Xie, 2016: The SCM Concept and Creation of ARM Forcing  
24 993 Datasets. *Meteorological Monographs*, **57**, 24.1-24.12, doi:10.1175/AMSMONOGRAPHS-D-15-0040.1.  
25  
26 994 Zhang, Y., and S. A. Klein, 2010: Mechanisms Affecting the Transition from Shallow to Deep  
27 995 Convection over Land: Inferences from Observations of the Diurnal Cycle Collected at the ARM  
28 996 Southern Great Plains Site. *Journal of the Atmospheric Sciences*, **67**, 2943-2959,  
29 997 10.1175/2010JAS3366.1.  
30  
31 998 Zhu, P., and Coauthors, 2005: Intercomparison and Interpretation of Single-Column Model Simulations  
32 999 of a Nocturnal Stratocumulus-Topped Marine Boundary Layer. *Monthly Weather Review*, **133**, 2741-  
33 1000 2758, 10.1175/mwr2997.1.

1001

1  
2  
3 1002 Table Captions:

4 1003 Table 1: Participating models and their basic information

5 1004 Table 2: Deep convective parameterizations in the participating SCMs

6  
7 1005 Table 3: Model information for sensitivity study.

8  
9 1006

10  
11 1007 Figure Captions:

12 1008 Figure 1: (Top) the composite diurnal cycle timeseries and (bottom) the harmonic dial plots of  
13 1009 total precipitation averaged for the long-term simulation periods at (left) SGP and (right) MAO.  
14 1010 The gray shading in the timeseries indicates  $1.96\times$  standard error (95% confidence) of the  
15 1011 observed precipitation. The radius and phase of the harmonic dial plots represent the amplitude  
16 1012 (mm/day) and the peak hour (LST), respectively, of the first Fourier component of DCP.

17  
18 1013 Figure 2: As in Figure 1 but for (left) wet season (December – March) and (right) dry season  
19 1014 (July – October) at MAO.

20  
21 1015 Figure 3: Diurnal cycle of cloud fraction from observations and simulations at (left) SGP and  
22 1016 (right) MAO.

23  
24 1017 Figure 4: The relationship between precipitation and CRH for (left) SGP and (right) MAO: (top)  
25 1018 the precipitation amount averaged for each CRH bin; (middle) the probability of precipitation  
26 1019 exceeding 1 mm/day for each CRH bin; (bottom) the occurrence frequency of each CRH bin.  
27 1020 CRH is binned in intervals of 2%.

28  
29 1021 Figure 5: Diurnal cycle timeseries of (top) total precipitation rate, (middle) convective  
30 1022 precipitation fraction, and (bottom) harmonic dial plots of total precipitation averaged for the  
31 1023 selected afternoon precipitation days during the long-term simulation periods at (left) SGP and  
32 1024 (right) MAO.

33  
34 1025 Figure 6: Percentage of days that the diurnal maximum precipitation occurs at each hour. The  
35 1026 total number of cases are 136 days for SGP and 111 days for MAO.

36  
37 1027 Figure 7: (Top) apparent heating ( $Q_1$ ) and (bottom) drying ( $Q_2$ ) averaged between 12 and 20 LST  
38 1028 for selected afternoon precipitation days during the long-term simulation periods at (left) SGP  
39 1029 and (right) MAO.

40  
41 1030 Figure 8: The mean (dot, circle or diamond), median (cross), 25<sup>th</sup> and 75<sup>th</sup> percentiles (vertical  
42 1031 lines) of precipitation onset time for the afternoon precipitation days at (left) SGP and (right)  
43 1032 MAO. Models for sensitivity studies in Section 4 are also shown here in thin lines.

44  
45 1033 Figure 9: As in Figure 5 but for selected nocturnal precipitation days.

46  
47  
48  
49  
50  
51  
52  
53  
54  
55  
56  
57  
58  
59  
60

1  
2  
3 1034 Figure 10: Precipitation rates from different components in CMC model for selected nocturnal  
4 1035 precipitation days.

6 1036 Figure 11:  $Q_1$  and  $Q_2$  averaged between 00 and 06 LST for selected nocturnal precipitation days  
8 1037 at (left) SGP and (right) MAO.

10 1038 Figure 12: As in Figure 5 but for selected models/configurations for sensitivity study. Sensitivity  
11 1039 runs are indicated by dashed/dotted lines and open symbols. Note that the convective  
12 1040 precipitation fraction for EAMv1.SILHS (blue dotted line) is zero because the convective and  
13 1041 large-scale precipitation is unified in CLUBB-SILHS.

16 1042 Figure 13: As in Figure 12 but for nocturnal precipitation days.

18 1043 Figure 14: The diurnal cycle of (top) surface latent heat, (middle) sensible heat fluxes and  
19 1044 (bottom) ground heat flux (net radiative fluxes minus latent and sensible heat fluxes) averaged  
20 1045 for the long-term simulation periods at (left) SGP and (right) MAO. The diurnal cycle averaged  
21 1046 in afternoon and nocturnal precipitation days have similar performance (not shown).

24 1047  
25  
26  
27  
28  
29  
30  
31  
32  
33  
34  
35  
36  
37  
38  
39  
40  
41  
42  
43  
44  
45  
46  
47  
48  
49  
50  
51  
52  
53  
54  
55  
56  
57  
58  
59  
60

Table 1: Participating models and their basic information

<b>Model name</b>	<b>Full name</b>	<b>Vertical levels</b>	<b>Timestep</b>	<b>turbulence</b>	<b>Stratiform clouds</b>	<b>Shallow convection</b>	<b>References</b>	<b>Contact Person</b>
<b>EAMv1</b>	The E3SM* Atmospheric Model V1	72	30min	CLUBB	MG2, CLUBB	CLUBB	Rasch et al. (2019); Bogenschutz et al. (2020)	Shaocheng Xie, Shuaiqi Tang
<b>EAMv1.trigger**</b>	EAMv1 with revised convective trigger	72	30min	CLUBB	MG2, CLUBB	CLUBB	Xie et al. (2019)	Shaocheng Xie, Shuaiqi Tang
<b>EAMv1.SILHS</b>	EAMv1 with CLUBB- SILHS	72	30min	CLUBB	MG2, CLUBB- SILHS	CLUBB- SILHS	Guo et al. (2021)	Vincent Larson, Zhun Guo
<b>SCAM6</b>	Single Column Atmosphere Model Version 6	32	20min	CLUBB	MG2, CLUBB	CLUBB	Gottelman et al. (2019)	Shuaiqi Tang
<b>SCAM5</b>	Single Column Atmosphere Model Version 5	30	20min	UW- diag_TKE	MG, Park1	UW-PB09	Neale et al. (2012)	Shuaiqi Tang
<b>SAM0-UNICON</b>	Seoul National University Atmosphere Model	30	20min	UW- diag_TKE	MG, Park2	UNICON	Park et al. (2019)	Sungsu Park, Jihoon Shin
<b>SKIM</b>	Single Column Korean Integrated Model	64	10min	Shin-Hong	WSM5, PCH16	HanPan	Hong et al. (2013); Hong et al. (2018)	Myung-Seo Koo, Song-You Hong
<b>CMC</b>	Canadian Meteorological Center	84	450sec	TKE1.5	Sundqvist	M-Bechtold	McTaggart-Cowan et al. (2019a)	Paul Vaillancourt, Jing Yang
<b>SMCPCP</b>	Stochastic MultiCloud Plume Convective Parameterization	30	20min	HB	MG, Park1	Unified Stochastic Plume-ZM	Khouider et al. (2021)	Boualem Khouider, Phani Murali Krishna
<b>TaiESM1</b>	Taiwan Earth System Model Version 1	30	30min	UW- diag_TKE	MG, GTS	UW-PB09	Lee et al. (2020)	Yi-Chi Wang
<b>ICON</b>	Icosahedral Nonhydrostatic Weather and Climate Model	90	2min	Raschendorf er00	Seifert08, Köhler20	Bechtold14	Zängl et al. (2015); Bařák Ďurán et al. (2021)	Martin Köhler, Daniel Klocke

\*the full names and references of the acronyms and physical schemes are given in the Appendix.

\*\*The results of EAMv1.trigger, EAMv1.SILHS and SCAM5 are only shown in the sensitivity studies in Section 4.

Table 2: Deep convective parameterizations in the participating SCMs

Model name	Deep convection	closure	Convective trigger	downdraft	reference
<b>EAMv1</b>	Zhang-McFarlane scheme (ZM)	Dilute CAPE	(1) CAPE >70 J/kg (2) The air parcel launch level is chosen within the boundary layer	Starts from updraft-top mass flux	Xie et al. (2018)
<b>EAMv1.t rigger</b>	ZM with revised convective trigger	Dilute CAPE	(1) CAPE >0 (2) dCAPE >0 (3) The air parcel launch level is chosen between the surface and 600 hPa	Same as EAMv1	Xie et al. (2019)
<b>EAMv1.S ILHS</b>	CLUBB-SILHS	No explicit closure	Not needed	Rain evaporation affect fluxes	Thayer-Calder et al. (2015); Griffin and Larson (2016)
<b>SCAM6</b>	ZM	Dilute CAPE	(1) CAPE >70 J/kg (2) The air parcel launch level is chosen within the boundary layer	Downdraft starts from updraft-top mass flux	Gottelman et al. (2019)
<b>SCAM5</b>	ZM	Dilute CAPE	Same as SCAM6	Same as SCAM6	Neale et al. (2012)
<b>SAM0-UNICON</b>	UNICON	No explicit closure	Not needed	Downdraft generated from updraft	Park (2014a, 2014b)
<b>SKIM</b>	KSAS	Quasi-equilibrium closure considering boundary-layer forcing	(1) $P_{\text{parcel\_start}} - P_{\text{LFC}} < P_{\text{crit}}(\text{RH}_{\text{low}})$ (2) $P_{\text{LFC\_w/o\_ent}} - P_{\text{LFC\_w/ent}} < 25 \text{ hPa}$ (3) $\text{CIN} < -120 \text{ m}^2 \text{ s}^{-2}$ (4) cloud depth > 150 hPa (5) cloud work function > 0	Starts from the level of minimum moist static energy between LFC and 450 hPa	Han et al. (2020)
<b>CMC</b>	Modified Kain-Fritsch (KF) with a mid-level elevated convective scheme	CAPE	(1) mixed parcel from PBL lifted to LCL to which a temperature perturbation is added is buoyant (2) cloud depth > 3000 m	Initiated at level of free sink	Kain and Fritsch (1990, 1992); McTaggart-Cowan et al. (2020)
<b>SMCPCP</b>	Unified Stochastic Plume-ZM	Weighted kinetic energy and CAPE	Same as SCAM6	Same as SCAM6	Khouider et al. (2021)
<b>TaiESM1</b>	ZM with revised convective trigger	Dilute CAPE	(1) CAPE >70 J/kg (2) $P_{\text{parcel\_start}} - P_{\text{LFC}} < 150 \text{ hPa}$ (3) The air parcel launch level is chosen between the surface and 600 hPa	Same as SCAM6	Wang and Hsu (2019)
<b>ICON</b>	Bechtold14	CAPE	Entraining parcels starting with levels up to 350hPa above the surface that must detect cloud layer thicker than 200hPa.	Starts from Level of Free Sinking (LFS) $M(\text{LFS}) = -0.3M(\text{up,base})$	Bechtold et al. (2014)

Table 3: Model information for sensitivity study.

Model name	Model features	Reference
<b>EAMv1</b>	Deep convection: ZM with convective trigger: (1) CAPE >70 J/kg (2) The air parcel launch level is chosen within the boundary layer	
<b>EAMv1.trigger</b>	Deep convection: ZM with convective trigger: (1) CAPE >0 (2) dCAPE >0 (3) The air parcel launch level is chosen between the surface and 600 hPa	Xie et al. (2019)
<b>EAMv1.SILHS</b>	Deep convection: CLUBB-SILHS	Thayer-Calder et al. (2015); Larson (2017)
<b>SAM0-UNICON</b>	Turbulence: diag_TKE Stratiform clouds: MG, Park1 Shallow Convection: UNICON Deep convection: UNICON	Park et al. (2019)
<b>SCAM6</b>	Turbulence: CLUBB Stratiform clouds: MG2, CLUBB Shallow Convection: CLUBB Deep convection: ZM	Gettelman et al. (2019)
<b>SCAM5</b>	Turbulence: diag_TKE Stratiform clouds: MG, Park1 Shallow Convection: PB09 Deep convection: ZM	Neal et al. (2012)
<b>SCAM6.land</b>	Interactive land	
<b>SKIM.land</b>	Interactive land	
<b>SKIM.nudge</b>	Nudging temperature and moisture	

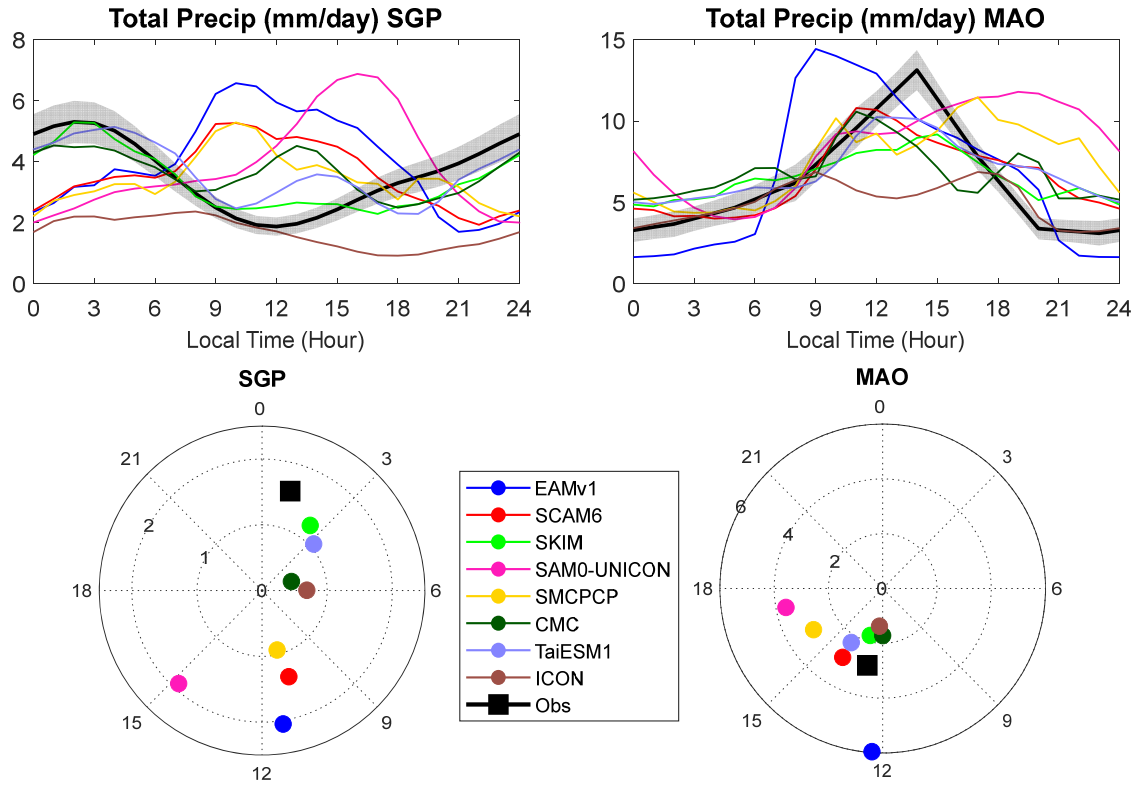


Figure 1: (Top) the composite diurnal cycle timeseries and (bottom) the harmonic dial plots of total precipitation averaged for the long-term simulation periods at (left) SGP and (right) MAO. The gray shading in the timeseries indicates  $1.96\times$  standard error (95% confidence) of the observed precipitation. The radius and phase of the harmonic dial plots represent the amplitude (mm/day) and the peak hour (LST), respectively, of the first Fourier component of DCP.

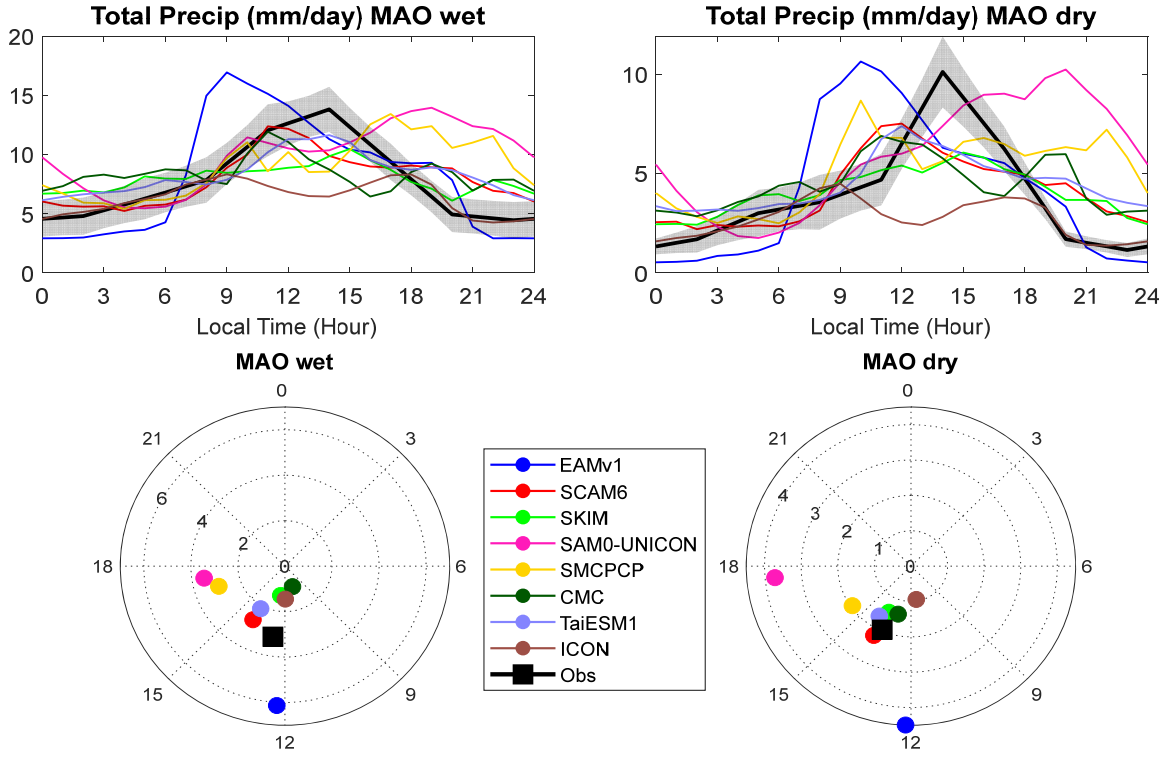


Figure 2: As in Figure 1 but for (left) wet season (December – March) and (right) dry season (July – October) at MAO.

1  
2  
3  
4  
5  
6  
7  
8  
9  
10  
11  
12  
13  
14  
15  
16  
17  
18  
19  
20  
21  
22  
23  
24  
25  
26  
27  
28  
29  
30  
31  
32  
33  
34  
35  
36  
37  
38  
39  
40  
41  
42  
43  
44  
45  
46  
47  
48  
49  
50  
51  
52  
53  
54  
55  
56  
57  
58  
59  
60

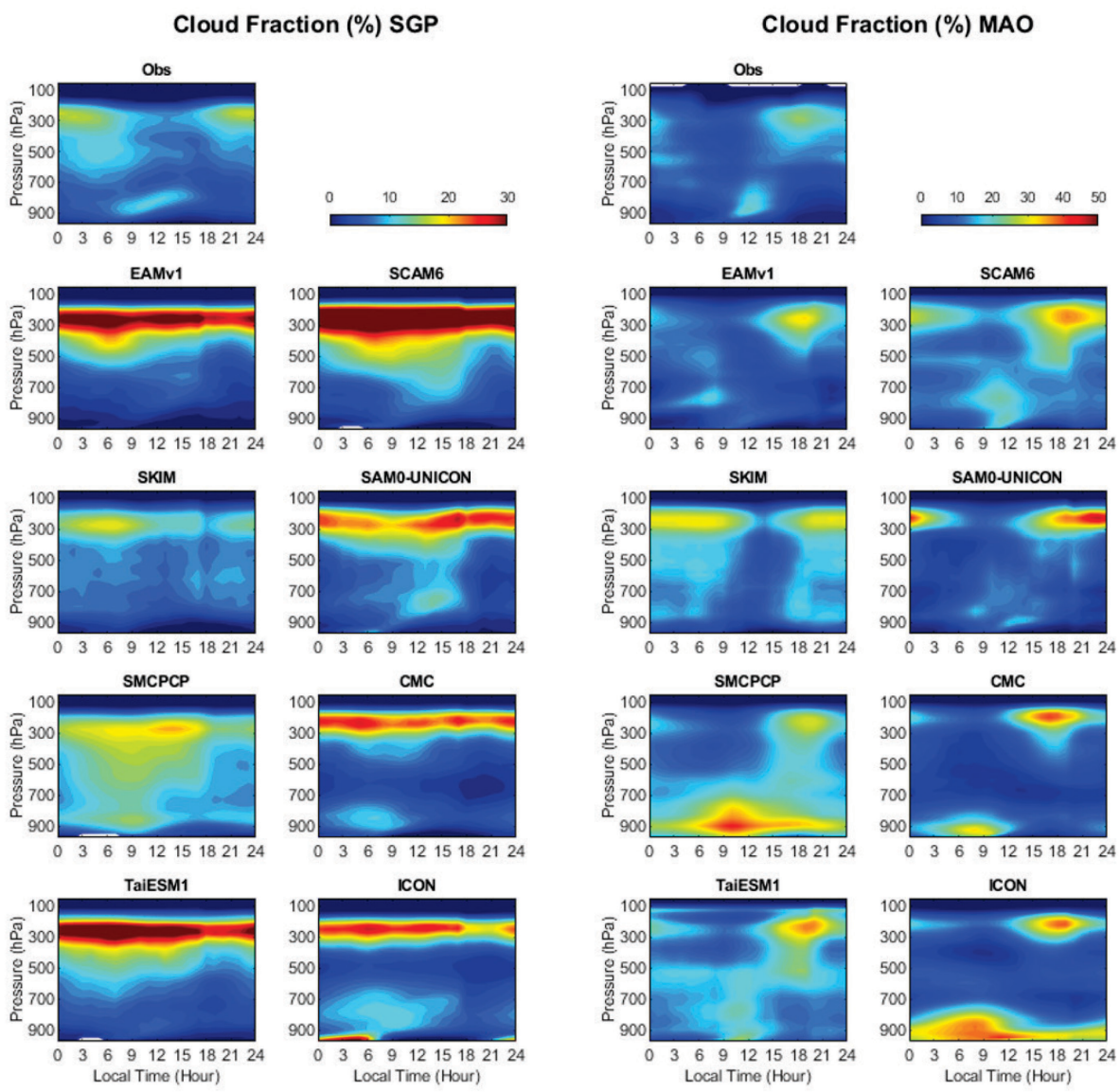


Figure 3: Diurnal cycle of cloud fraction from observations and simulations at (left) SGP and (right) MAO.

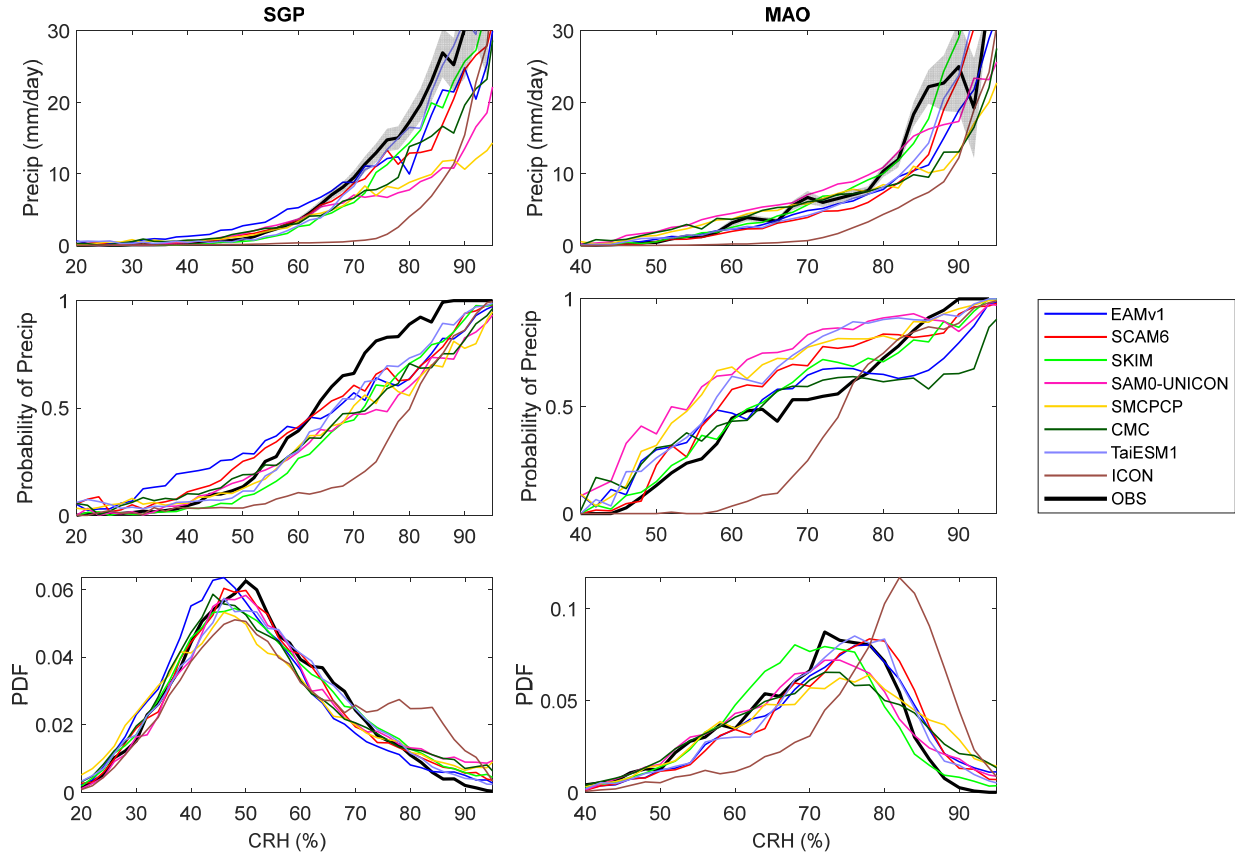


Figure 4: The relationship between precipitation and CRH for (left) SGP and (right) MAO: (top) the precipitation amount averaged for each CRH bin; (middle) the probability of precipitation exceeding 1 mm/day for each CRH bin; (bottom) the occurrence frequency of each CRH bin. CRH is binned in intervals of 2%.

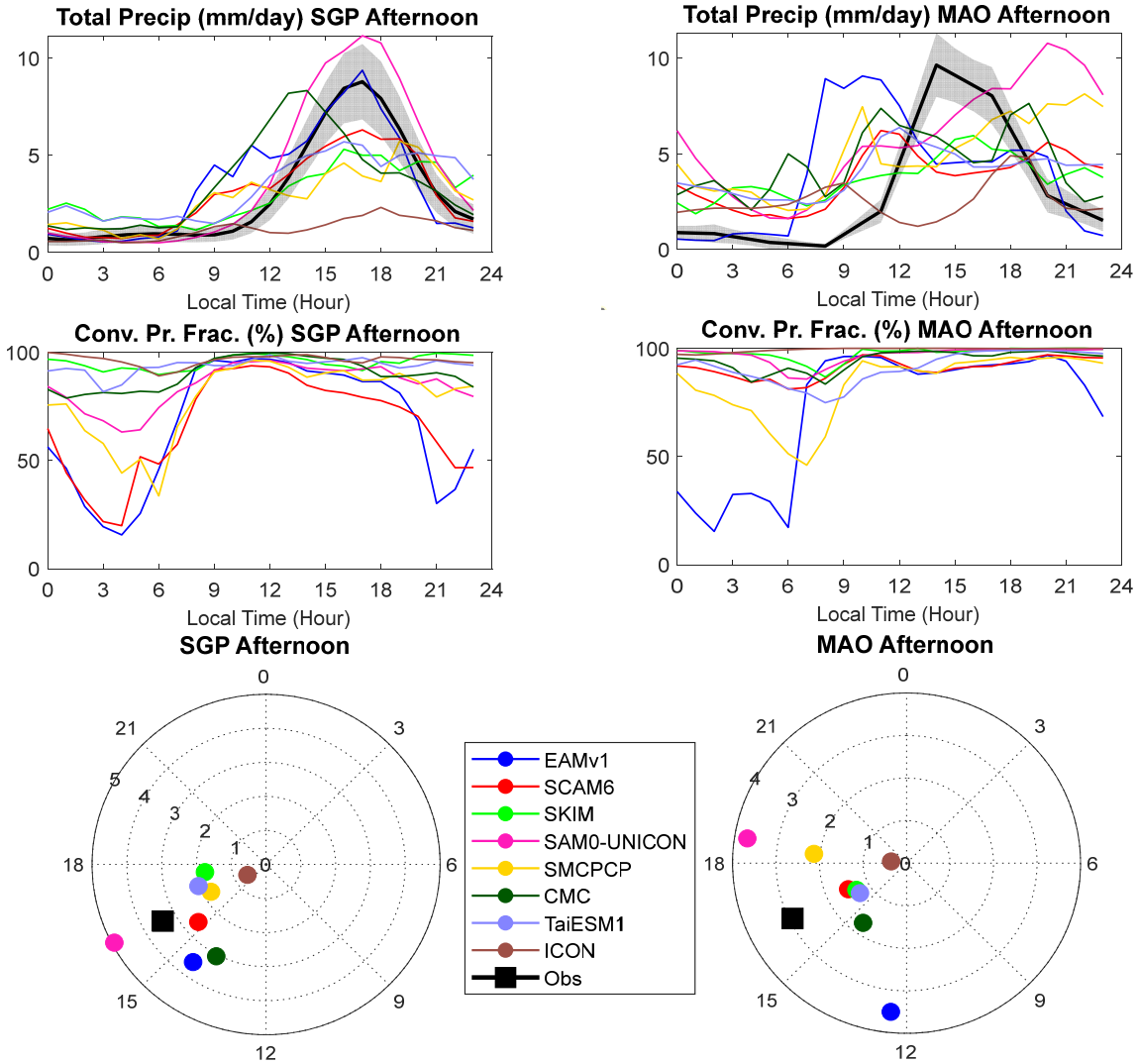


Figure 5: Diurnal cycle timeseries of (top) total precipitation rate, (middle) convective precipitation fraction, and (bottom) harmonic dial plots of total precipitation averaged for the selected afternoon precipitation days during the long-term simulation periods at (left) SGP and (right) MAO.

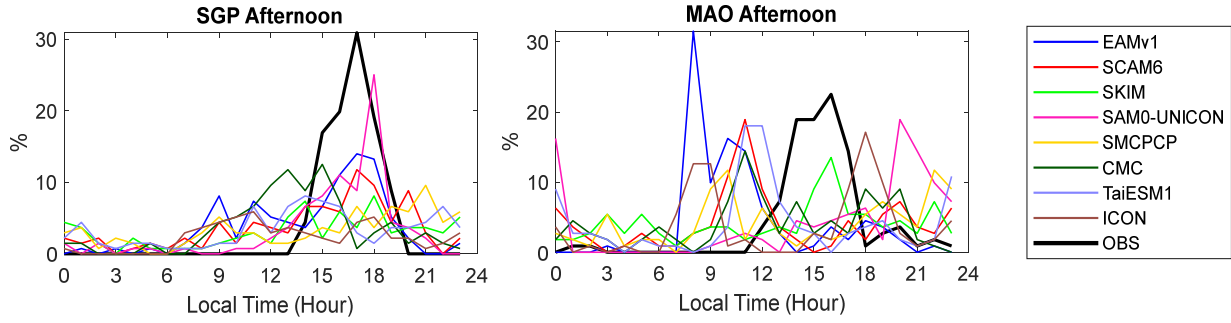


Figure 6: Percentage of days that the diurnal maximum precipitation occurs at each hour. The total number of cases are 136 days for SGP and 111 days for MAO.

1  
2  
3  
4  
5  
6  
7  
8  
9  
10  
11  
12  
13  
14  
15  
16  
17  
18  
19  
20  
21  
22  
23  
24  
25  
26  
27  
28  
29  
30  
31  
32  
33  
34  
35  
36  
37  
38  
39  
40  
41  
42  
43  
44  
45  
46  
47  
48  
49  
50  
51  
52  
53  
54  
55  
56  
57  
58  
59  
60

1  
2  
3  
4  
5  
6  
7  
8  
9  
10  
11  
12  
13  
14  
15  
16  
17  
18  
19  
20  
21  
22  
23  
24  
25  
26  
27  
28  
29  
30  
31  
32  
33  
34  
35  
36  
37  
38  
39  
40  
41  
42  
43  
44  
45  
46  
47  
48  
49  
50  
51  
52  
53  
54  
55  
56  
57  
58  
59  
60

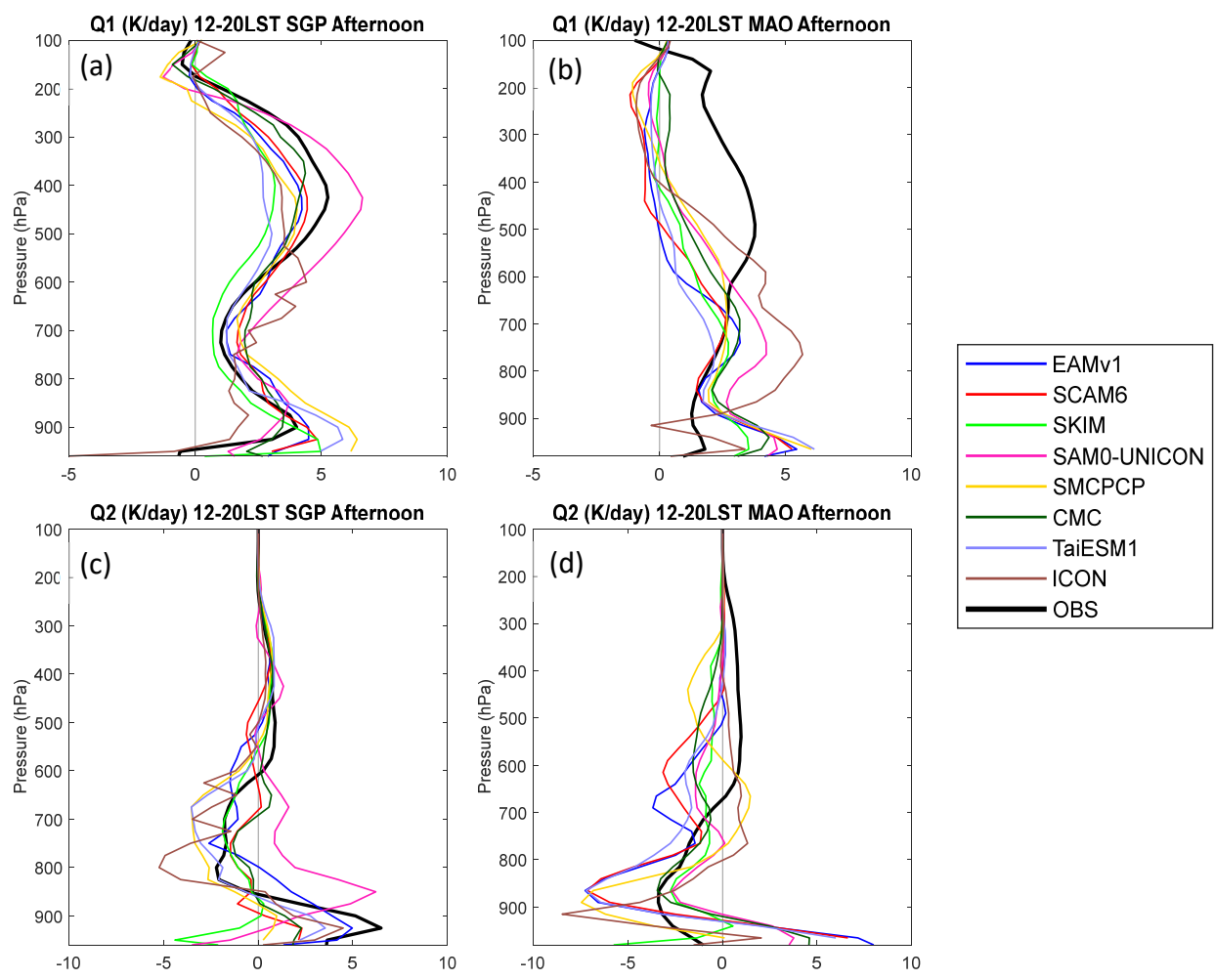


Figure 7: (Top) apparent heating ( $Q_1$ ) and (bottom) drying ( $Q_2$ ) averaged between 12 and 20 LST for selected afternoon precipitation days during the long-term simulation periods at (left) SGP and (right) MAO.

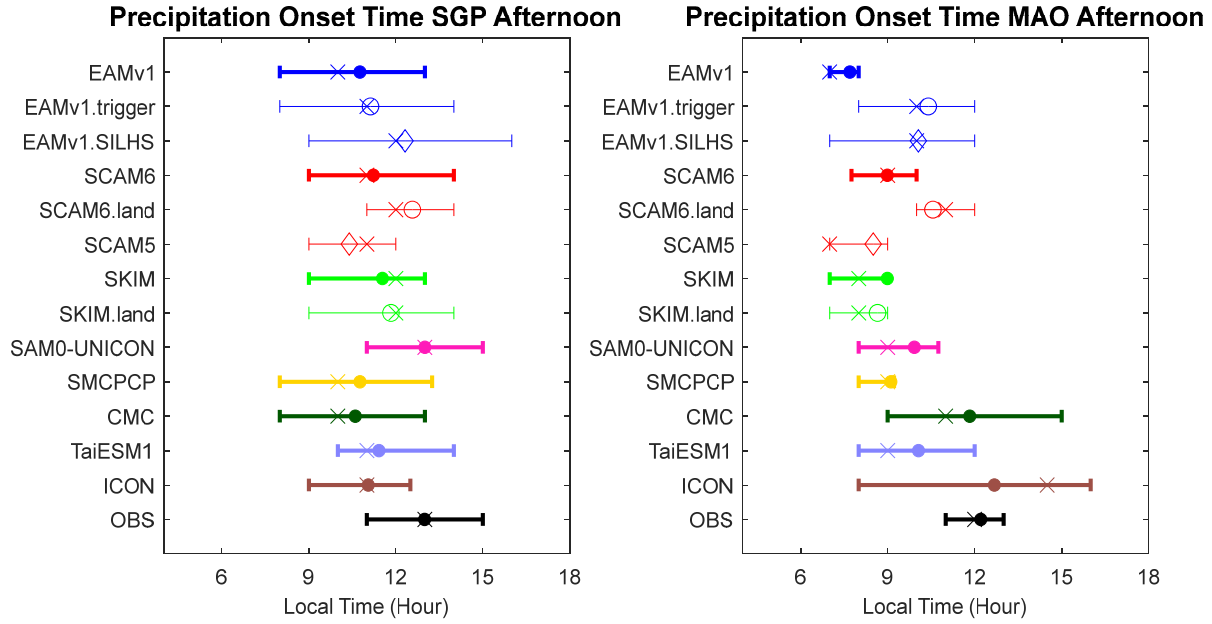


Figure 8: The mean (dot, circle or diamond), median (cross), 25<sup>th</sup> and 75<sup>th</sup> percentiles (vertical lines) of precipitation onset time for the afternoon precipitation days at (left) SGP and (right) MAO. Models for sensitivity studies in Section 4 are also shown here in thin lines.

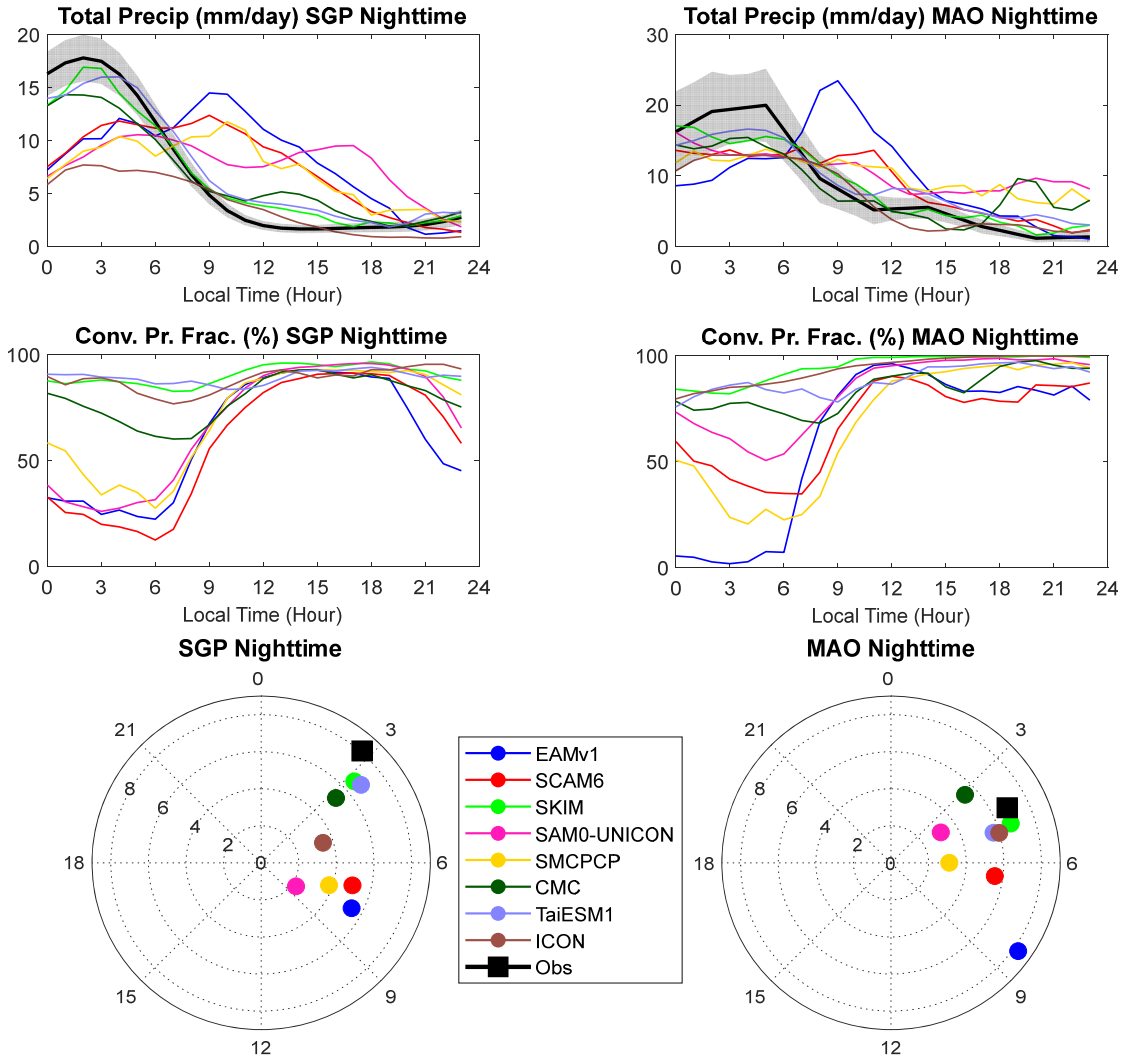


Figure 9: As in Figure 5 but for selected nocturnal precipitation days.

1  
2  
3  
4  
5  
6  
7  
8  
9  
10  
11  
12  
13  
14  
15  
16  
17  
18  
19  
20  
21  
22  
23  
24  
25  
26  
27  
28  
29  
30  
31  
32  
33  
34  
35  
36  
37  
38  
39  
40  
41  
42  
43  
44  
45  
46  
47  
48  
49  
50  
51  
52  
53  
54  
55  
56  
57  
58  
59  
60

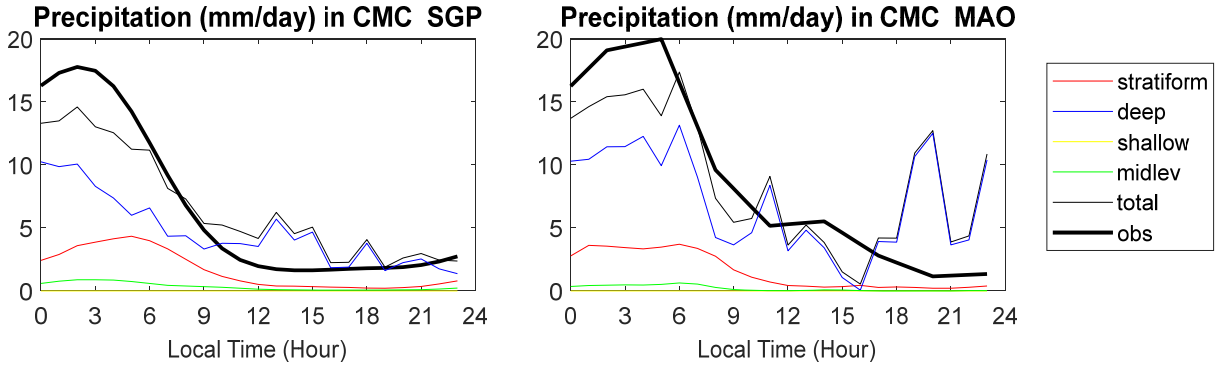


Figure 10: Precipitation rates from different components in CMC model for selected nocturnal precipitation days.

1  
2  
3  
4  
5  
6  
7  
8  
9  
10  
11  
12  
13  
14  
15  
16  
17  
18  
19  
20  
21  
22  
23  
24  
25  
26  
27  
28  
29  
30  
31  
32  
33  
34  
35  
36  
37  
38  
39  
40  
41  
42  
43  
44  
45  
46  
47  
48  
49  
50  
51  
52  
53  
54  
55  
56  
57  
58  
59  
60

1  
2  
3  
4  
5  
6  
7  
8  
9  
10  
11  
12  
13  
14  
15  
16  
17  
18  
19  
20  
21  
22  
23  
24  
25  
26  
27  
28  
29  
30  
31  
32  
33  
34  
35  
36  
37  
38  
39  
40  
41  
42  
43  
44  
45  
46  
47  
48  
49  
50  
51  
52  
53  
54  
55  
56  
57  
58  
59  
60

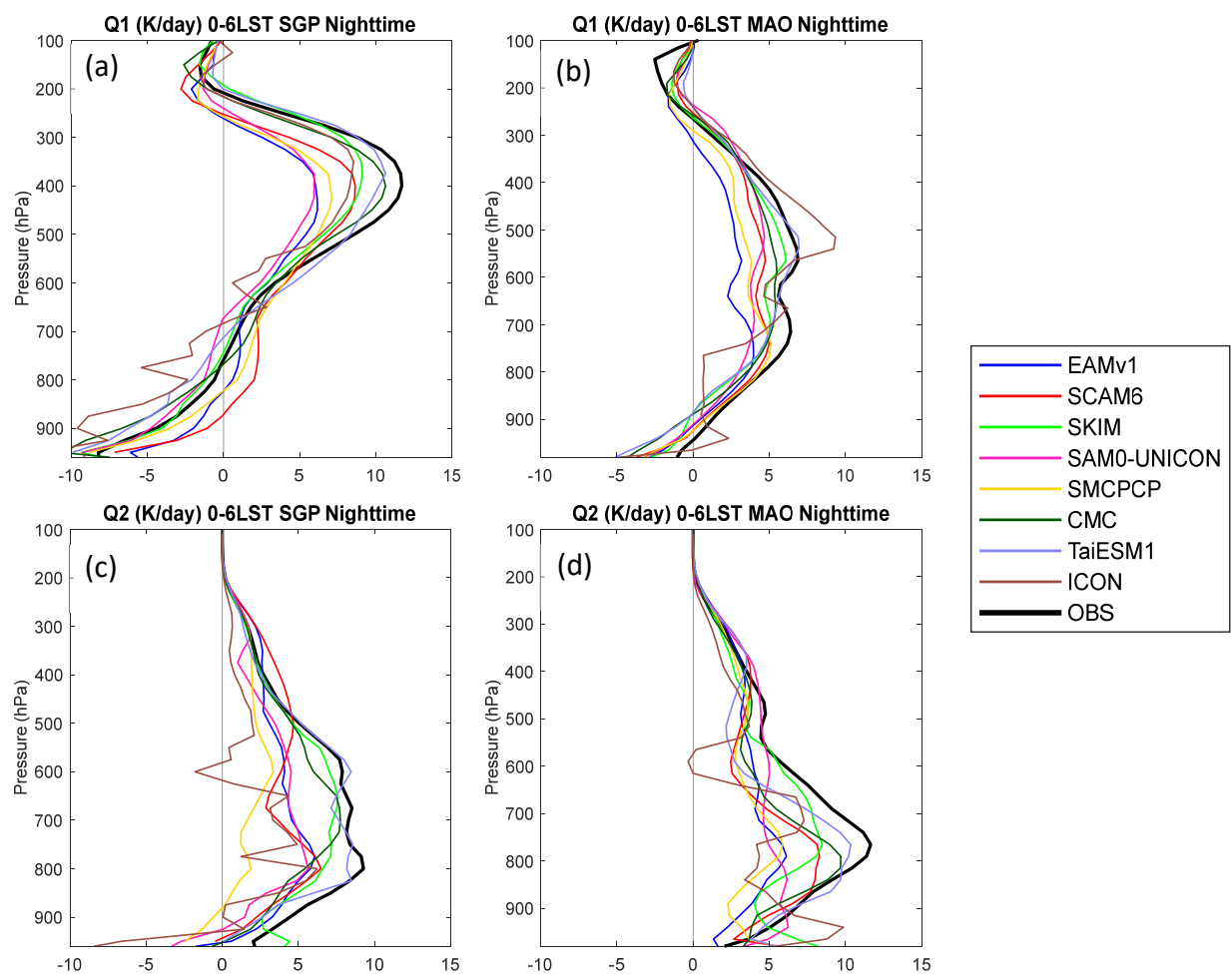


Figure 11: Q<sub>1</sub> and Q<sub>2</sub> averaged between 00 and 06 LST for selected nocturnal precipitation days at (left) SGP and (right) MAO.

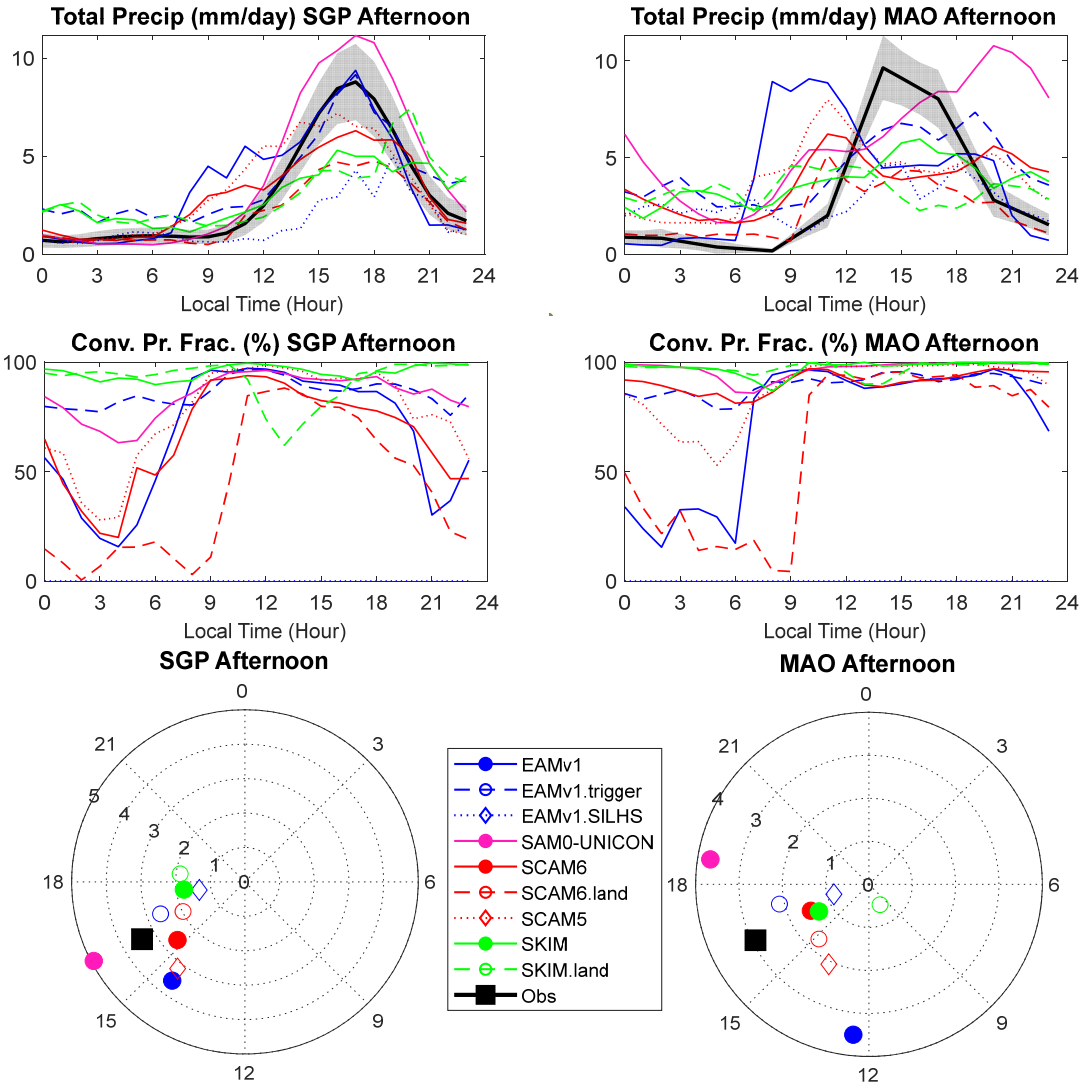


Figure 12: As in Figure 5 but for selected models/configurations for sensitivity study. Sensitivity runs are indicated by dashed/dotted lines and open symbols. Note that the convective precipitation fraction for EAMv1.SILHS (blue dotted line) is zero because the convective and large-scale precipitation is unified in CLUBB-SILHS.

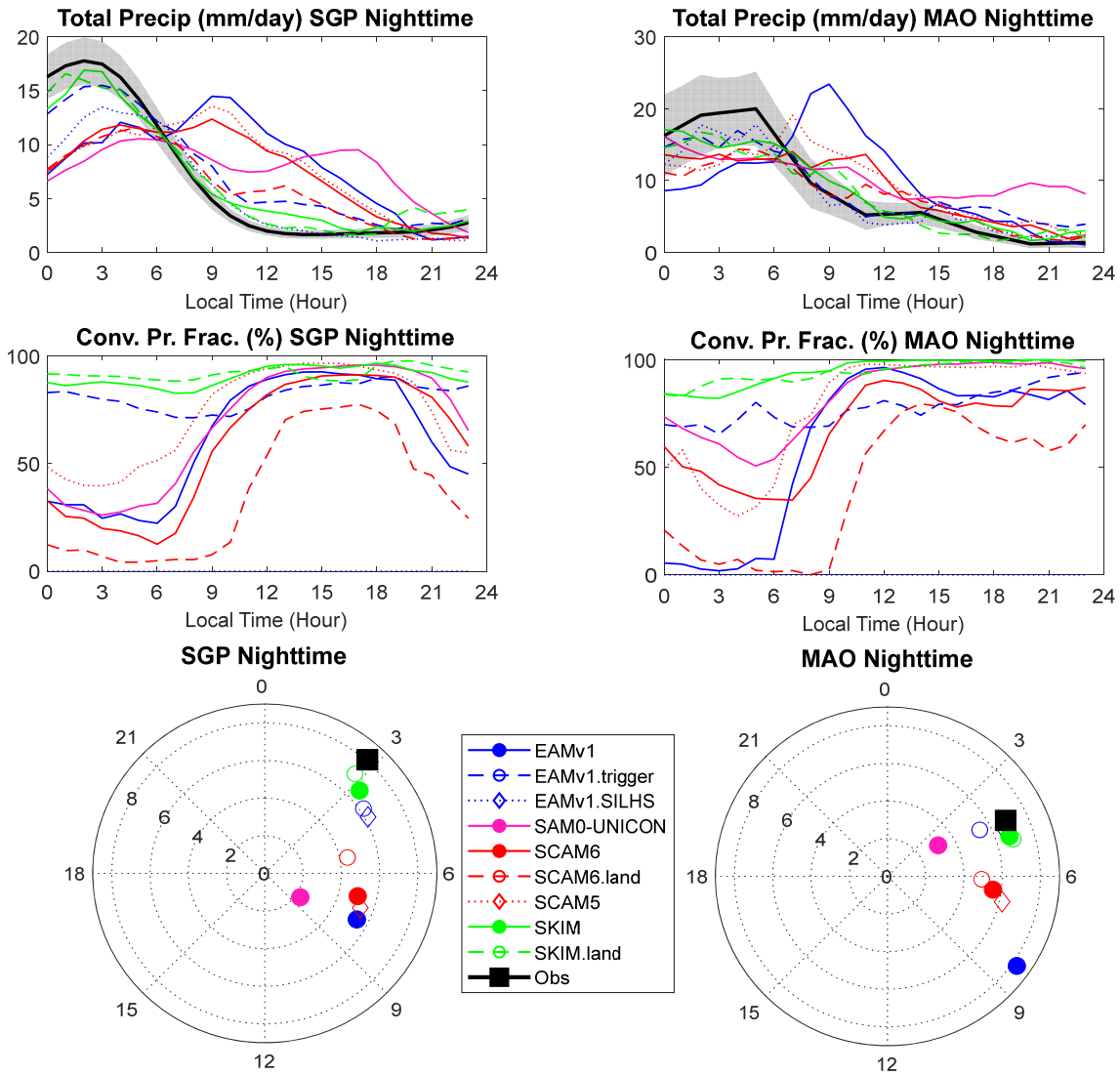


Figure 13: As in Figure 12 but for nocturnal precipitation days.

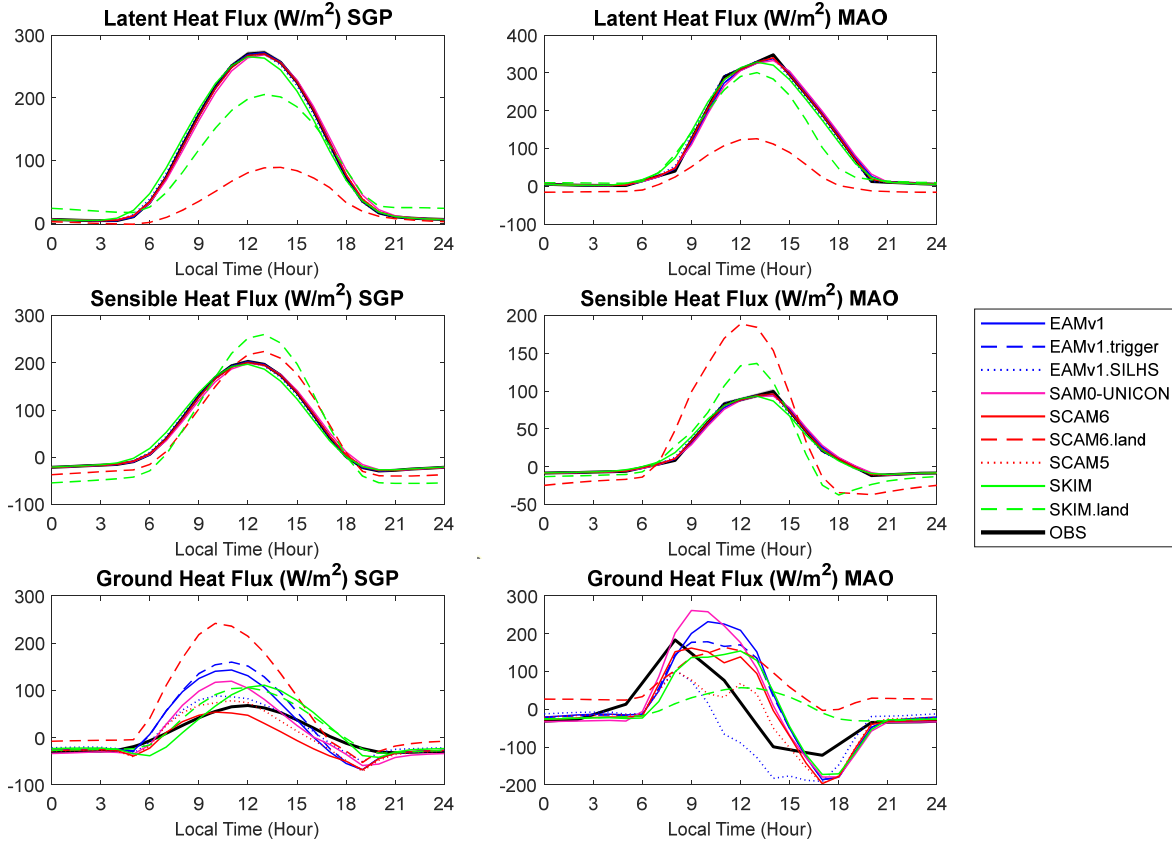


Figure 14: The diurnal cycle of (top) surface latent heat, (middle) sensible heat fluxes and (bottom) ground heat flux (net radiative fluxes minus latent and sensible heat fluxes) averaged for the long-term simulation periods at (left) SGP and (right) MAO. The diurnal cycle averaged in afternoon and nocturnal precipitation days have similar performance (not shown).